

ORACLE-CT: Anatomy-Aware Support Pooling for CT Classification

Lavsen Dahal^{a,b,*}, Yubraj Bhandari^{a,c}, Geoffrey Rubin^d and Joseph Y. Lo^{a,b,**}

^aCenter for Virtual Imaging Trials, RAI Labs, Department of Radiology, Duke University, Durham, 27708, North Carolina, USA

^bElectrical and Computer Engineering, Pratt School of Engineering, Duke University, Durham, 27708, North Carolina, USA

^cDepartment of Mathematics, Trinity College of Arts & Sciences, Duke University, Durham, 27708, North Carolina, USA

^dDepartment of Radiology and Imaging Sciences, University of Arizona College of Medicine, Tucson, 85004 Arizona, USA

ARTICLE INFO

Keywords:

Computed tomography
multi-label classification
multiple instance learning
anatomical priors
foundation models
external validation

ABSTRACT

Abdominal CT disease classification is challenging because each examination is a large three-dimensional study with multiple possible findings, while diagnostic evidence is often localized to specific organs or anatomical compartments. Most study-level CT classifiers aggregate spatial encoder features using anatomy-agnostic operators such as global average pooling or unrestricted attention, allowing evidence for each label to be drawn from the full feature lattice. This creates a mismatch between anatomy-structured disease evidence and anatomy-agnostic evidence aggregation. We propose **ORACLE-CT**, an encoder-agnostic anatomy-aware aggregation framework that uses multi-organ segmentation to define label-specific anatomical supports and restricts attention pooling to those supports. ORACLE-CT supports single-organ, multi-organ union, comparative, localized, and global support strategies, enabling disease-specific evidence aggregation.

We evaluate ORACLE-CT across three representation families: a generic pretrained Vision Transformer (DINOv3), a native 3D convolutional network (I3D-ResNet-121), and a radiology-native foundation encoder (Pillar-0). Models are trained end-to-end on MERLIN and evaluated internally and under frozen external transfer to Duke-Abdomen and AMOS. Compared with global average pooling, support-masked pooling improved MERLIN macro-AUROC/AUPRC from 0.838/0.638 to 0.858/0.676 for DINOv3 and from 0.829/0.617 to 0.848/0.659 for I3D-ResNet-121. On the harmonized 10-label external evaluation, support-masked pooling also improved transfer for DINOv3 on Duke-Abdomen (AUROC/AUPRC: 0.802/0.628 to 0.835/0.683) and AMOS (0.742/0.313 to 0.762/0.350), with similar gains for I3D-ResNet-121. For Pillar-0, most improvement arose from learned attention itself, with smaller additional gains from support-masked pooling. These results show that enforcing anatomical support at pooling time improves discrimination and external robustness while preserving an auditable link between disease predictions and anatomical evidence.

1. Introduction

Abdominal CT is one of the most common and information-rich imaging examinations in clinical practice, but its increasing use has also contributed substantially to radiology workload [28, 38, 42, 30]. This has motivated growing interest in automated interpretation of abdominal CT examinations, where clinically relevant findings may be numerous, co-occurring, and distributed across a large three-dimensional volume [34, 1]. A central challenge is that diagnostically relevant evidence is not uniformly distributed across the scan, but is often anatomically anchored to specific organs, compartments, or inter-organ relationships [40, 36, 29]. Effective CT interpretation therefore requires not only strong local image features, but also a principled mechanism for aggregating spatial evidence into examination-level decisions.

In this work, we focus on one scalable formulation of automated abdominal CT interpretation: multi-label classification of clinically relevant findings from abdominal CT examinations. Recent progress has made this formulation increasingly feasible at scale. Volumetric encoders and radiology foundation models now provide strong

*Corresponding author

**Principal corresponding author

✉ lavsen.dahal@duke.edu (L. Dahal); yubraj.bhandari@duke.edu (Y. Bhandari); grubin@arizona.edu (G. Rubin); joseph.lo@duke.edu (J.Y. Lo)

ORCID(s): 0000-0002-8991-759X (L. Dahal); 0009-0004-7279-4097 (Y. Bhandari); 0000-0002-3820-2500 (G. Rubin); 0000-0002-9540-5072 (J.Y. Lo)

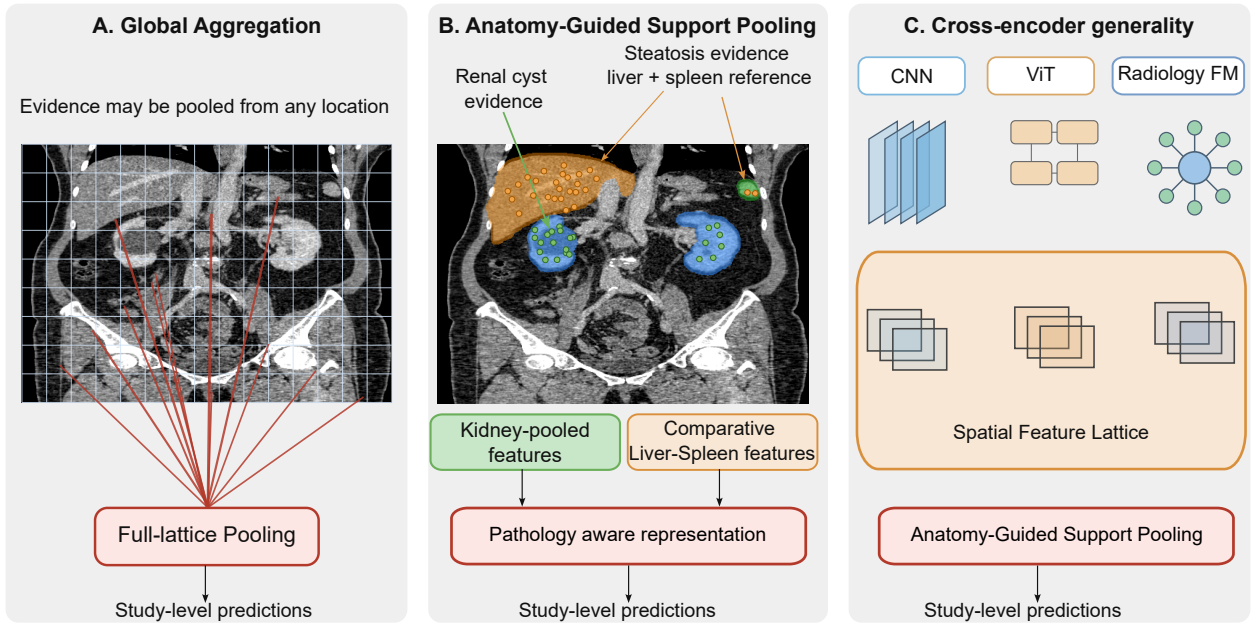


Figure 1: Conceptual overview of ORACLE-CT. (A) Standard study-level classification commonly pools over the full spatial feature lattice, potentially mixing pathology-relevant and irrelevant anatomy. (B) ORACLE-CT assigns each pathology to anatomically appropriate support and pools features only within that support, producing pathology-aware representations such as kidney-pooled features for renal cyst and liver-spleen pooled features for hepatic steatosis. (C) This anatomy-guided support-pooling principle is encoder-agnostic and can be instantiated on top of CNN, Vision Transformer, and radiology foundation model feature lattices.

spatial representations [31, 43, 5, 22]. In parallel, natural language processing and large language model-assisted report extraction have made it increasingly practical to derive examination-level labels from radiology reports across large imaging datasets [27, 32, 19, 13]. At the same time, robust multi-organ segmentation has become practical across large CT datasets, providing coarse organ and compartment maps that can serve as anatomical supports [45, 9, 35, 39]. Together, these developments create an opportunity for anatomically structured CT classification: strong spatial features, scalable examination-level supervision, and anatomical support maps are now available within a common modeling pipeline.

However, the availability of these components does not by itself specify how local image evidence should be converted into examination-level predictions. Modern CT classification pipelines typically pair a spatial encoder with an aggregation operator that summarizes local features for each target finding [12, 24]. In practice, this step is often anatomy-agnostic: convolutional models commonly use global average pooling [23] over the final feature map, while Transformer-based models may use a learned class token that summarizes the full token sequence [11], or unrestricted attention over the entire spatial feature lattice. In such designs, evidence for a given finding can be drawn from the full volume unless anatomical support is explicitly imposed.

Such generic aggregation can be mismatched to abdominal CT, where the relevant anatomical support varies across findings. Renal cysts and hydronephrosis are primarily kidney-centered [36]; hepatic steatosis is commonly assessed using hepatic attenuation and, in some protocols, liver-spleen attenuation ratio [14, 29]; and ascites or metastatic disease may require evidence from broader but still anatomically constrained regions [7, 26]. Thus, aggregation is not simply a generic pooling step, but a central modeling choice. This motivates anatomy-aware classification strategies that guide evidence aggregation using organ and compartment supports.

We address this problem with **ORACLE-CT**, an encoder-agnostic aggregation framework for study-level CT classification. ORACLE-CT keeps the full-volume encoder unchanged, but changes where the classifier is allowed to pool spatial evidence for each finding. Each label is assigned to a clinically motivated anatomical support. Pooling is then performed within the assigned support rather than indiscriminately over the entire feature lattice. In this way,

anatomical structure is introduced at the representation-formation stage, while preserving compatibility with diverse CT encoders.

To isolate the role of anatomical support, we evaluate ORACLE-CT under a controlled head-comparison protocol against anatomy-agnostic aggregation baselines. For each encoder family, the backbone, preprocessing, and optimization protocol are held fixed while only the aggregation mechanism is varied, separating the effect of label-specific support restriction from generic changes in pooling capacity. We test this principle across three encoder families: a natural-image pretrained Vision Transformer, a native 3D CNN, and a radiology-native foundation encoder. Figure 1 illustrates the contrast between anatomy-agnostic global aggregation and pathology-specific support pooling.

This work makes four main contributions:

1. We propose a modular support-masked aggregation head that can be attached to heterogeneous CT encoders and trained end-to-end without cropping the input volume or modifying the encoder architecture.
2. We define a clinically motivated support taxonomy for abdominal CT findings, spanning single-organ, multi-organ union, comparative, localized, and global supports, enabling organ-specific, relational, and diffuse findings to be modeled within a unified framework.
3. We introduce a controlled aggregation comparison that separates anatomy-agnostic pooling from anatomy-aware support pooling while keeping the encoder family, preprocessing, and optimization protocol fixed within each backbone.
4. We validate ORACLE-CT on MERLIN and two external datasets, Duke-Abdomen and AMOS, showing improved internal performance and frozen external transfer across generic transformer, native 3D CNN, and radiology-native foundation-model representations.

2. Related Work

Supervised study-level CT classification. Large-scale supervised CT classification studies have shown that multi-label disease prediction from volumetric CT is feasible, while also highlighting persistent challenges in weak supervision, missing labels, class imbalance, calibration, and external validation [12, 40]. Prior work has also incorporated anatomical structure by dividing CT interpretation across body regions, for example using separate models or classifiers for different anatomical regions or organ systems [40]. These approaches demonstrate the value of anatomical information for CT disease classification, but they primarily use anatomy to partition the input space or specialize prediction models. They leave open a complementary question: when a shared full-volume encoder is used, how should spatial features be aggregated into label-specific study-level predictions? This question is especially relevant for scalable multi-label systems, where a single encoder pass may need to support many findings whose evidence arises from different anatomical supports.

CT report supervision, vision-language models, and foundation encoders. Recent CT representation learning methods have focused on building stronger image encoders by pretraining on large-scale CT datasets, often using paired CT volumes and radiology reports through contrastive, generative, or multimodal objectives [15, 22, 5, 34, 1, 21, 20, 17, 3, 43]. These approaches have enabled CT vision-language models and radiology foundation encoders that can support downstream classification through zero-shot prompting, linear probing, or end-to-end fine-tuning. Their central strength is improved spatial representation learning and transfer across CT tasks. However, once a spatial feature representation has been extracted, study-level classification still requires an aggregation mechanism that determines how local features are summarized into finding-specific predictions.

Aggregation, multiple instance learning, and anatomical priors. In large-scale CT classification, labels are often available for the entire examination, while the relevant image evidence may occupy only a subset of the volume. The model must therefore summarize many local token or voxel features into one prediction for each finding. This setting is closely related to multiple instance learning (MIL), where a bag of spatial instances is mapped to a global label under weak supervision [10, 18, 48].

Learned attention pooling provides a flexible way to weight spatial instances before forming an examination-level representation [18, 2, 25, 46]. However, when applied without anatomical constraints, attention pooling still learns weights over the full feature lattice and does not specify which regions are clinically appropriate for a given prediction. This motivates aggregation strategies that retain full-volume encoding while incorporating anatomical support into the pooling stage.

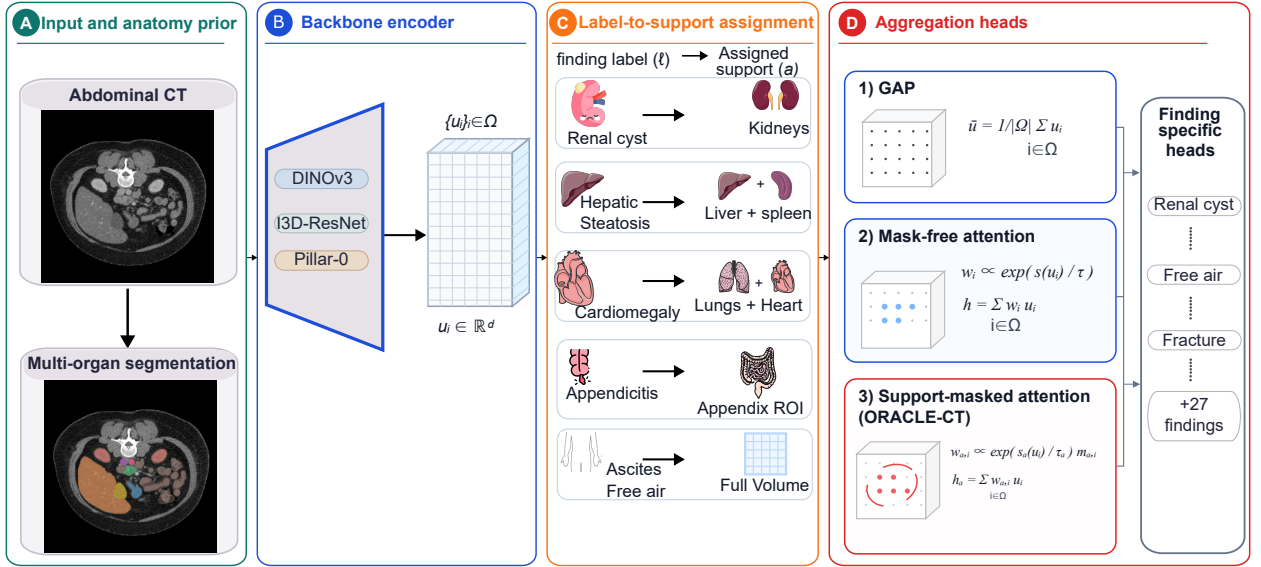


Figure 2: Overview of ORACLE-CT anatomy-aware support pooling. ORACLE-CT modifies the aggregation stage of multi-label CT classification while leaving the encoder architecture unchanged. Each backbone is trained separately, but within a given backbone the same full-volume encoder provides features for all labels. (A) An abdominal CT volume is paired with a multi-organ segmentation, which provides coarse anatomical supports. (B) A pretrained CT encoder maps the full volume to a spatial feature lattice $\{u_i\}_{i \in \Omega}$. ORACLE-CT is encoder-agnostic and is evaluated separately with DINOv3, I3D-ResNet-121, and Pillar-0. (C) Each finding label is assigned to a predefined anatomical support, such as a single organ, a comparative multi-organ support, a union support, a localized region, or the full volume when global context is appropriate. (D) Three aggregation heads are compared under the same training protocol: global average pooling uniformly averages the full lattice; mask-free attention pooling learns content-weighted aggregation over all locations; and support-masked attention pooling normalizes attention only within the label-specific anatomical support. The resulting support-aware representations are passed to finding-specific classification heads for study-level multi-label prediction.

3. Method: ORACLE-CT

Figure 2 summarizes ORACLE-CT. We consider supervised multi-label CT classification, where a single CT volume is used to predict a set of finding labels. At a high level, ORACLE-CT decomposes this task into three components: (i) a pretrained encoder that maps the input volume to a dense spatial feature lattice, (ii) segmentation-derived anatomical supports assigned to finding labels, and (iii) an aggregation head that pools evidence within the assigned support before classification.

This decomposition isolates the effect of anatomy-aware aggregation by holding the encoder family and training protocol fixed within each backbone, and yields support-restricted pooling weights that can be qualitatively audited.

3.1. Problem Setup

A CT volume is represented as $X \in \mathbb{R}^{D \times H \times W}$. We consider a supervised multi-label classification problem with L finding labels. Ground-truth targets are $y \in \{0, 1, -1\}^L$, where -1 denotes a missing or unknown label. An encoder E_θ extracts spatial features from the volume, and an aggregation pathway A_ϕ maps these features to label logits $z \in \mathbb{R}^L$:

$$z = A_\phi(E_\theta(X)), \quad \hat{\mathbf{p}} = \text{sigmoid}(z) \in [0, 1]^L.$$

Here, A_ϕ denotes the full aggregation pathway, including label-to-support assignment, support-aware pooling, and finding-specific classification heads. Our focus is how this pathway should use segmentation-derived anatomical supports to convert spatial encoder features into anatomically meaningful multi-label predictions.

3.2. Encoders as Feature Lattices

As illustrated in Figure 2B, ORACLE-CT treats each backbone as a feature-lattice generator and applies the same downstream aggregation logic to the resulting spatial representation. Let Ω denote the index set of the encoder's final

spatial feature lattice, and let $\{u_i\}_{i \in \Omega}$, with $u_i \in \mathbb{R}^d$, denote the local features consumed by the aggregation head. The construction of Ω depends on the encoder substrate, but all pooling modes operate only on the resulting spatial features. This abstraction makes ORACLE-CT compatible with heterogeneous CT encoders while isolating the contribution of the aggregation head.

In this work, we validate ORACLE-CT across three representative backbone families: (i) a pseudo-3D token lattice produced by applying a 2D transformer to axial tri-slice inputs (DINOv3 [37]; after dropping non-spatial tokens), (ii) a voxel lattice produced by a native 3D CNN (I3D-ResNet-121) [16, 6], and (iii) a spatial activation lattice produced by a radiology-native foundation encoder (Pillar-0) [1] evaluated under its native preprocessing and recommended input geometry. We write $i \in \Omega$ for a lattice location, whether it corresponds to a token or a voxel-like spatial cell, and flatten coordinates for brevity.

DINOv3 provides a strong generic pretrained transformer encoder without radiology-specific pretraining. Because DINOv3 is a 2D vision transformer, we used a 2.5D tri-slice implementation: each axial center slice c was represented as a three-channel image using adjacent slices ($c-1, c, c+1$), resized to 224×224 , ImageNet-normalized, and processed independently by the pretrained encoder. After removing the class token and DINOv3 register tokens, the remaining spatial patch tokens were reassembled across sampled axial positions to form a pseudo-3D token lattice. Support masks were aligned using the same axial centers: the corresponding mask center slices were extracted, resized with nearest-neighbor interpolation to the DINOv3 input resolution, and downsampled to the patch-token grid for support-masked softmax pooling.

I3D-ResNet-121 represents a native 3D convolutional architecture for volumetric feature extraction and corresponds to the visual encoder family used in the MERLIN vision-language model [5]. We include this backbone to test whether ORACLE-CT improves downstream multi-label classification when built on a MERLIN-style volumetric image encoder. For this backbone, the CT volume was processed directly as a 3D tensor, and the final convolutional feature map was treated as a voxel lattice, with each spatial cell corresponding to one instance u_i . Segmentation-derived support masks were resampled with nearest-neighbor interpolation to the same feature-map resolution before pooling.

Pillar-0 represents a radiology-native foundation encoder pretrained at scale on CT data. Pillar-0 provides both a global pooled feature vector and a spatial activation map. The GAP baseline used the pooled output, whereas mask-free attention pooling and support-masked pooling operated on the spatial activation map after resampling segmentation-derived supports to the activation lattice. Thus, despite differences in architecture and pretraining, all three encoders are interfaced through the same ORACLE-CT abstraction: a spatial feature lattice followed by an aggregation head. This setup lets us test whether the value of explicit anatomy-aware aggregation depends on encoder inductive bias and pretraining domain.

3.3. Organ Groups, Anatomical Supports, and Label Anchoring

We introduce an explicit anatomy prior through segmentation-derived masks and a fixed label-to-support assignment. Figure 2A shows the segmentation-derived anatomy prior, while Figure 2D summarizes the representative support types used across disease labels.

Organ groups. Raw segmentation classes C are merged into a smaller set of clinically meaningful *organ groups* \mathcal{O} (e.g. left/right kidneys \rightarrow kidneys). For each raw class $c \in C$, let $S_c \in \{0, 1\}^{D \times H \times W}$ denote its binary mask. Let $\pi : C \rightarrow \mathcal{O}$ map raw classes to groups and define the group mask

$$M_o = \bigvee_{c: \pi(c)=o} S_c \in \{0, 1\}^{D \times H \times W}, \quad o \in \mathcal{O}.$$

We dilate M_o by r_o mm in metric space to absorb boundary uncertainty, then resample the mask to the encoder lattice Ω to obtain indicators $m_{o,i} \in \{0, 1\}$ and support

$$\Omega_o = \{i \in \Omega : m_{o,i} = 1\}.$$

Label anchoring and anatomical supports. Rather than mapping each label directly to a single organ, ORACLE-CT maps each disease label to a predefined anatomical support. Let \mathcal{A} denote the set of support definitions, where each support $a \in \mathcal{A}$ may correspond to a single organ, a union of organs, a comparative multi-organ support, a localized anatomical region, or the full volume. Each label $\ell \in \{1, \dots, L\}$ is assigned to one support through a fixed map

$$\kappa : \{1, \dots, L\} \rightarrow \mathcal{A}.$$

This induces support-specific label sets

$$\mathcal{L}_a = \{\ell : \kappa(\ell) = a\}.$$

For each support a , we construct a binary lattice mask $m_{a,i} \in \{0, 1\}$ when the support is mask-defined. Labels assigned to the same support share the corresponding pooled representation, while predictions remain disease-specific through separate output units in the support-specific classifier head. Global labels use the full lattice without an anatomical mask. For mask-defined supports, we denote the corresponding lattice index set by

$$\Omega_a = \{i \in \Omega : m_{a,i} = 1\}.$$

3.4. From Feature Lattices to ORACLE Heads

Given $\{u_i\}_{i \in \Omega}$, we compare three encoder-compatible aggregation heads in a staged ladder (Figure 2B) to isolate the effect of content weighting and anatomy priors: **(i) GAP** (Eq. 1), **(ii) mask-free attention pooling** (Eqs. 2–3), and **(iii) support-masked attention pooling** (Eqs. 4–6).

3.4.1. Mask-free Heads

Global Average Pooling (GAP). The simplest baseline summarizes the entire feature lattice uniformly:

$$h = \frac{1}{|\Omega|} \sum_{i \in \Omega} u_i \in \mathbb{R}^d, \quad z = W^{\text{global}} h + b^{\text{global}} \in \mathbb{R}^L. \quad (1)$$

Here $W^{\text{global}} \in \mathbb{R}^{L \times d}$ and $b^{\text{global}} \in \mathbb{R}^L$. GAP is feature-only, $\mathcal{O}(|\Omega|)$, and serves as our supervised baseline.

Mask-free attention pooling (unary baseline). To move beyond uniform pooling, we assign a learned weight to each lattice location using a lightweight *unary* scorer, followed by softmax normalization over the full lattice:

$$\alpha_i = s_{\text{pool}}(u_i), \quad w_i = \frac{\exp(\alpha_i/\tau)}{\sum_{j \in \Omega} \exp(\alpha_j/\tau)}, \quad \tau > 0, \quad (2)$$

$$h = \sum_{i \in \Omega} w_i u_i \in \mathbb{R}^d, \quad z = W^{\text{global}} h + b^{\text{global}} \in \mathbb{R}^L. \quad (3)$$

The scorer $s_{\text{pool}} : \mathbb{R}^d \rightarrow \mathbb{R}$ is a small per-location map (Linear($d \rightarrow 1$) on tokens or $1 \times 1 \times 1$ Conv3D on voxels). The weights satisfy $w_i \geq 0$ and $\sum_{i \in \Omega} w_i = 1$. Compared with GAP, mask-free attention pooling learns a content-weighted mixture while remaining mask-free and encoder-compatible.

Note: This is attention *pooling* via unary scoring and softmax normalization, not Transformer-style Q/K/V feature mixing [41, 44]. It is included specifically to decouple content-weighted pooling from the anatomical masking used by ORACLE-CT.

3.4.2. Support-masked Head

Support-masked attention pooling. For each anatomical support $a \in \mathcal{A}$, we apply a support-specific unary scorer $s_a : \mathbb{R}^d \rightarrow \mathbb{R}$ and temperature $\tau_a > 0$:

$$\alpha_{a,i} = s_a(u_i). \quad (4)$$

For mask-defined supports, attention is normalized only over locations inside the support using a masked softmax:

$$w_{a,i} = \frac{\exp(\alpha_{a,i}/\tau_a) m_{a,i}}{\sum_{j \in \Omega} \exp(\alpha_{a,j}/\tau_a) m_{a,j} + \varepsilon}, \quad \varepsilon > 0. \quad (5)$$

The support-specific pooled representation and logits are then

$$h_a = \sum_{i \in \Omega} w_{a,i} u_i, \quad z_a = W^{(a)} h_a + b^{(a)} \in \mathbb{R}^{|\mathcal{L}_a|}. \quad (6)$$

Table 1

Abdominal CT datasets and standard input geometry. Counts reflect patient-disjoint splits. MERLIN served as the internal development dataset, while Duke–Abdomen and AMOS were used only for external evaluation. For frozen transfer, calibration parameters and operating thresholds were selected on MERLIN validation and applied unchanged to the external datasets. For the standard DINOv3 and I3D–ResNet-121 experiments, CT volumes were clipped to $[-1000, 1000]$ HU, min–max normalized to $[0, 1]$, and resampled to the common geometry shown below. Pillar-0 was evaluated using its native 11-window input representation and input geometry, as described in Table 3. Duke–Abdomen shares 27 labels with MERLIN, and AMOS shares a 10-label subset used for three-way evaluation.

Dataset	Train	Val	Test	Labels	Resampled Spacing (mm)	Shape
MERLIN (internal)	15,175	5,018	5,082	30	$3 \times 1.5 \times 1.5$	$160 \times 224 \times 224$
Duke–Abdomen (external)	—	—	2,000	27	$3 \times 1.5 \times 1.5$	$160 \times 224 \times 224$
AMOS (external)	—	—	1,107	10	$3 \times 1.5 \times 1.5$	$160 \times 224 \times 224$

Here $W^{(a)}$ and $b^{(a)}$ are classifier parameters for the disease labels assigned to support a .

For global supports, no anatomical mask is applied and the corresponding labels use the mask-free global attention head. If a mask-defined support Ω_a is empty after resampling to the encoder lattice, we instead use the mask-free global attention representation for labels assigned to that support. This fallback is applied before computing the support-specific pooled representation and prevents degenerate empty-support outputs when small organs or thin structures vanish after downsampling.

Composite and comparative supports. For union supports, the support mask $m_{a,i}$ is formed by the union of the component organ masks and pooling proceeds as in Eq. 6. For comparative supports, component organs are pooled separately and then concatenated before classification. For example, for hepatic steatosis,

$$h_{\text{steatosis}} = [h_{\text{liver}}; h_{\text{spleen}}], \quad z_{\text{steatosis}} = W_{\text{steatosis}} h_{\text{steatosis}} + b_{\text{steatosis}}.$$

This allows the classifier to use cross-organ information while preserving organ-specific pooling.

Support-masked attention differs from both GAP and mask-free attention in one crucial respect: the normalization domain is anatomically constrained. As a result, the pooled representation for each support-anchored disease label is formed only from locations within the assigned segmented support, encouraging study-level predictions to rely on anatomically appropriate support regions rather than unrestricted global context.

3.5. Training Objective

Loss with missing finding labels. We optimize binary cross-entropy only over findings with available study-level labels. Let $m_\ell = \mathbb{1}[y_\ell \neq -1]$ denote the label-availability mask for finding ℓ , where $y_\ell = -1$ indicates that the finding label is missing or uncertain. For available labels, $y_\ell \in \{0, 1\}$, and the per-study loss is

$$\mathcal{L} = \frac{1}{\sum_{\ell=1}^L m_\ell} \sum_{\ell=1}^L m_\ell \text{ BCEWithLogits}(z_\ell, y_\ell).$$

The BCE term was weighted using label-specific positive weights estimated from the MERLIN training split, with positive-weight ratios clipped at 10.

4. Experimental Design, datasets, and Evaluation Protocol

4.1. Datasets

Table 1 summarizes the abdominal CT datasets, split sizes, label spaces, and standard input geometry used for the DINOv3 and I3D–ResNet-121 experiments. Unless otherwise noted, intensities were clipped to $[-1000, 1000]$ HU and min–max normalized to $[0, 1]$.

MERLIN (internal development dataset). MERLIN is an abdomen-focused CT dataset with 30 study-level labels annotated as positive, negative, or missing/unknown [5]. We used the released patient-disjoint train/validation/test splits and treated MERLIN as the sole internal development dataset for model training, model selection, calibration, and threshold selection.

Duke–Abdomen (external clinical dataset). We additionally evaluated on a private abdominal CT dataset from Duke University Hospitals ($N=2,000$), with 27 study-level labels overlapping MERLIN. Duke–Abdomen was used only for frozen external evaluation, with no training, recalibration, or threshold tuning performed on this dataset. The Duke–Abdomen dataset was assembled from de-identified archival abdominal CT examinations with associated radiology reports under an approved Duke University Health System IRB protocol.

AMOS (external public dataset). We further evaluated on the public AMOS abdominal CT dataset ($N=1,107$), harmonized to a 10-label subset shared with MERLIN and Duke–Abdomen for three-way comparison.

4.2. Reference Labels and Label Harmonization

MERLIN labels were used as released with the dataset. For Duke–Abdomen, study-level reference labels were derived from radiology reports using two independent LLM-assisted NLP pipelines based on MedGemma [33] and Qwen [47], implemented within the RATE framework released with Pillar-0 [1]. Each pipeline extracted report findings and mapped them to the MERLIN study-level label space. Concordant positive or negative assignments were accepted as the final reference label, whereas disagreements or insufficient report evidence for a given finding were marked as missing/unknown and excluded for that finding.

For AMOS, we used the publicly released labels from the Foundation Models for General CT Image Diagnosis challenge [8]; no AMOS labels were modified or re-derived. Because label availability differed across datasets, evaluation was performed on the dataset-specific evaluable label set: 30 labels in MERLIN, 27 labels overlapping MERLIN in Duke–Abdomen, and 10 AMOS labels that could be unambiguously harmonized with MERLIN findings set. Macro-averaged performance was therefore reported within each dataset’s evaluable label set, while the shared 10-label subset was used for direct three-way comparison across MERLIN, Duke–Abdomen, and AMOS.

4.3. Segmentation and Findings-Specific Support Construction

Segmentation backbone. We obtained multi-organ segmentations using TotalSegmentator [45] as anatomical coordinate systems for defining label-specific support regions used during support-masked attention pooling.

Findings-specific anatomical supports. For each abdominal finding, we defined a support region according to the expected spatial organization of its imaging evidence rather than assigning all labels to a single fixed organ grouping scheme. Unless otherwise noted, mask-defined supports were dilated by 3 mm in metric space before pooling to reduce sensitivity to segmentation boundary uncertainty. The same label-to-support mapping was applied across MERLIN, Duke–Abdomen, and AMOS. No dataset-specific remapping or support redesign was performed for external evaluation; only the evaluable label subset differed across datasets. Table 2 summarizes the anatomical support definitions used for the abdominal findings.

4.4. Preprocessing and Augmentation

For the standard DINOv3 and I3D–ResNet-121 experiments, CT volumes were clipped to $[-1000, 1000]$ HU, min–max normalized to $[0, 1]$, and resampled to the voxel spacing and input shape listed in Table 1. Pillar-0 was evaluated using its native 11-window input representation and input geometry, as shown in Table 3. As Pillar-0 retains its native preprocessing pipeline, its results are reported throughout for contextual cross-encoder comparison rather than strict preprocessing-matched comparison. During MERLIN training, we used mild 3D augmentation consisting of small affine perturbations (in-plane rotation, translation, and scaling), gamma intensity jitter, and low-variance additive noise. Spatial flips were disabled along all axes to preserve anatomical laterality and organ correspondence (e.g., spleen-left versus liver-right).

4.5. Training Protocol

External datasets were never used for optimization, model selection, recalibration, or threshold tuning. To isolate the effect of study-level aggregation, all backbones were fine-tuned end-to-end on MERLIN under a harmonized training protocol, with only backbone-specific adjustments to learning rate, batch size, and memory-saving settings when required by input geometry.

We optimized a multi-label binary cross-entropy objective using AdamW with cosine learning-rate decay, mixed-precision training, and gradient clipping. For the standard ORACLE–CT experiments with DINOv3 and I3D–ResNet-121, models were trained for 20 epochs with a base learning rate of 3×10^{-4} , weight decay 10^{-4} , batch size 10, and 5 warm-up epochs. Grouped learning rates were used so that the classification head learned faster than the backbone, with

Table 2

Disease-specific anatomical supports used by ORACLE-CT. Each target finding is assigned a label-dependent support strategy defined from multi-organ segmentation. Unless otherwise noted, mask-defined supports were dilated by 3 mm before pooling; bone masks were not dilated, cardiomegaly used a larger-context cardiothoracic support, comparative supports used separate organ-wise pooling followed by feature concatenation, and global labels used no anatomical mask. For supports requiring contextual proxies, support definitions were fixed before model training and applied unchanged across datasets. Pleural-context support was constructed by dilating the lung masks to include adjacent pleural space. As direct appendix mask was unavailable, the appendicitis support was approximated using an appendix-focused lower-right bowel/cecal region.

Disease label(s)	Strategy	Support construction	Pooling behavior
Hepatomegaly	Single-organ	Liver support	Attention restricted to the liver mask
Splenomegaly	Single-organ	Spleen support	Attention restricted to the spleen mask
Abdominal aortic aneurysm	Single-organ	Aortic support	Attention restricted to the aorta mask
Gallstones	Single-organ	Gallbladder support	Attention restricted to the gallbladder mask
Hydronephrosis	Single-organ	Bilateral kidney support	Union of kidney_left and kidney_right masks
Renal hypodensities	Single-organ	Bilateral kidney support	Union of kidney_left and kidney_right masks
Atherosclerosis	Single-organ	Aortic support	Attention restricted to the aorta mask
Coronary calcification	Single-organ	Cardiac support	Attention restricted to the heart mask
Atelectasis	Single-organ	Lung support	Union of lung-lobe masks
Osteopenia, Fracture	Single-organ	Skeletal support	Union of available bone masks; no dilation applied
Pancreatic atrophy	Single-organ	Pancreatic support	Attention restricted to the pancreas mask
Prostatomegaly	Single-organ	Prostate support	Attention restricted to the prostate mask
Biliary ductal dilation	Union	Hepatobiliary-pancreatic support	Union of liver, gallbladder, and pancreas masks
Cardiomegaly	Union	Cardio-thoracic support	Union of heart and lung masks with larger-context dilation
Bowel obstruction, Submucosal edema	Union	Bowel support	Union of small_bowel and colon masks
Pleural effusion	Union	Lung + pleural-context support	Union of lung masks with pleural-space context/proxy region
Hiatal hernia	Union	Upper GI / thoracoabdominal junction support	Union of stomach and lung masks
Renal cyst	Union	Kidney + cyst support	Union of bilateral kidney masks with available kidney-cyst masks
Surgically absent gallbladder	Union	Gallbladder fossa support	Union of gallbladder and liver masks
Aortic valve calcification	Union	Aortic-root / cardiac support	Union of heart and aorta masks
Hepatic steatosis	Comparative	Liver vs spleen comparative support	Liver and spleen pooled separately, then concatenated before classification
Appendicitis	Localized	Appendix-focused subregion within bowel support	Localized appendix proxy derived from the bowel/cecal region
Thrombosis, Free air, Ascites, Anasarca, Metastatic disease, Lymphadenopathy	Global	Full-volume support	No anatomical mask applied; prediction uses the mask-free full-lattice attention head

head learning-rate scale = 3.0. Validation was performed every epoch, and the checkpoint with the highest validation macro-AUROC was retained for final testing.

Training used class-balanced positive weights derived from the MERLIN training split, with positive-weight ratios clipped at 10. Labels marked missing or unknown (−1) were excluded from both loss computation and evaluation.

All reported DINOv3 and I3D-ResNet-121 results were obtained by end-to-end fine-tuning rather than frozen-feature evaluation. For the Pillar-0 experiments, we retained the model’s native 11-window abdominal CT input representation and used a lower base learning rate (1×10^{-4}), shorter warm-up of 2 epochs, batch size 1 with gradient accumulation over 4 steps, and gradient checkpointing to accommodate the substantially larger 384^3 input volume.

4.6. Evaluation Metrics, Calibration, and Operating Points

We report threshold-free discrimination using macro-AUROC and macro-AUPRC, computed as unweighted averages over labels with available ground truth in each dataset. Labels marked missing or unknown were excluded from metric computation.

Table 3

Backbone-specific training settings. All models were fine-tuned end-to-end on MERLIN and selected by validation macro-AUROC.

Backbone	Input	Batch	LR	Warm-up	Notes
DINOv3	160×224×224	10	3×10^{-4}	5	AMP, AdamW, cosine decay
I3D-ResNet-121	160×224×224	10	3×10^{-4}	5	AMP, AdamW, cosine decay
Pillar-0	11×384 ³	1	1×10^{-4}	2	grad accum. 4, checkpointing

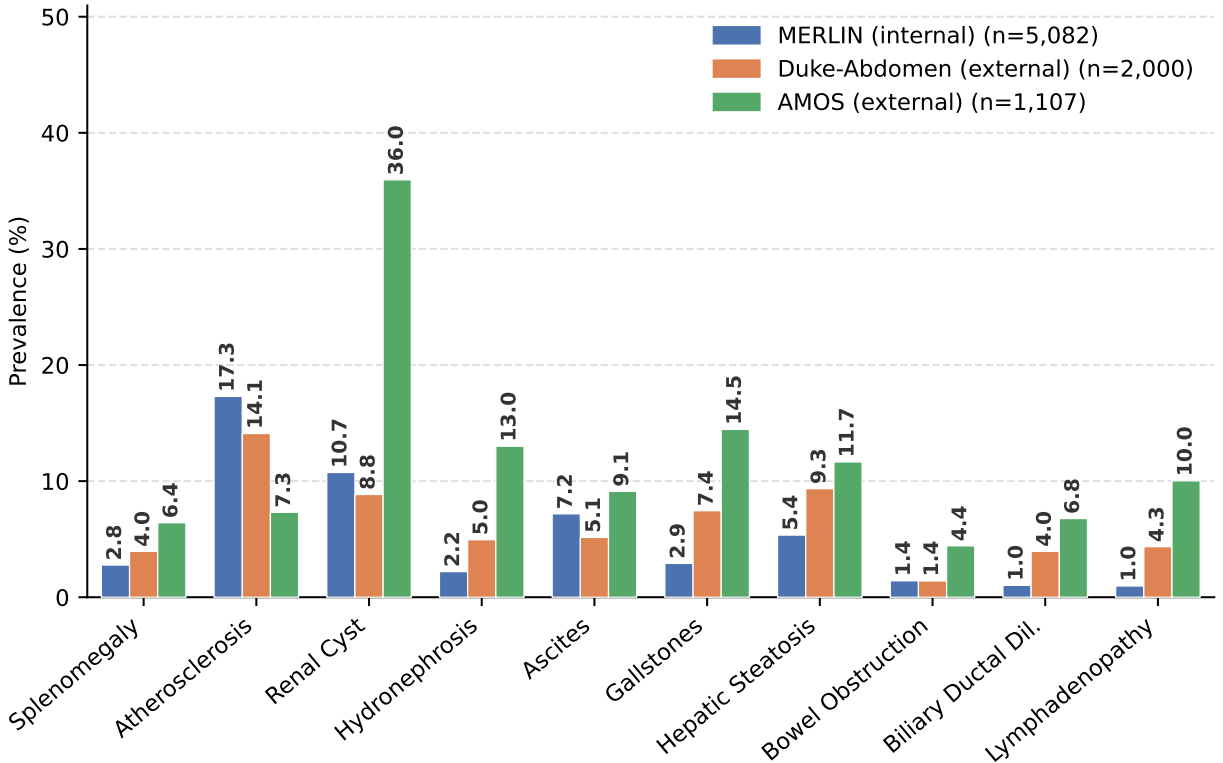


Figure 3: Prevalence of the harmonized label subset across test datasets. Per-label prevalence (%) for the labels shared across MERLIN (internal; $n = 5,082$), Duke-Abdomen (external; $n = 2,000$), and AMOS (external; $n = 1,107$). Marked prevalence differences remain across datasets despite label harmonization, indicating substantial dataset-level variation in case mix.

For threshold-dependent metrics, we applied temperature scaling on MERLIN validation and then selected per-model, per-label operating points by maximizing F1 score on the same split. F1 and balanced accuracy were both computed using these F1-optimized thresholds.

4.7. Label Prevalence and Distribution Shift

We analyzed label prevalence to characterize class imbalance in the internal dataset and findings-frequency shift across external abdomen datasets. MERLIN exhibited a long-tailed label distribution, with substantial variation in prevalence across findings and several relatively rare labels (Supplementary Figure S2). External evaluation was therefore performed not only under institutional shift, but also under nontrivial prevalence mismatch.

Figure 3 compares per-label prevalence across MERLIN, Duke-Abdomen, and AMOS for the harmonized 10-label subset used for three-way evaluation. Several findings showed marked prevalence differences between datasets, indicating that external transfer was assessed under genuine cross-dataset case-mix shift.

Table 4

Internal abdomen mode ablations on MERLIN across encoder families. Mode ablations on the MERLIN test split for a generic pretrained token backbone (DINOv3), a native 3D CNN (I3D-ResNet-121), and a radiology foundation encoder (Pillar-0). We compare uniform global average pooling, mask-free attention pooling, and support-masked pooling. Metrics are macro-averaged over the full MERLIN label set. Pillar-0 results are reported for contextual cross-encoder comparison (see 4.4). Point estimates are shown for readability. Full 95% bootstrap confidence intervals for all metrics are provided in Supplementary Table S1.

Backbone	Mode	AUROC	AUPRC	F1	BA
DINOv3	GAP baseline	0.8380	0.6382	0.6356	0.7302
	Mask-free attn pooling	0.8473	0.6617	0.6432	0.7263
	Support-masked pooling	0.8576	0.6763	0.6596	0.7471
I3D-ResNet-121	GAP baseline	0.8288	0.6169	0.6108	0.7124
	Mask-free attn pooling	0.8181	0.6086	0.6048	0.7104
	Support-masked pooling	0.8482	0.6587	0.6424	0.7427
Pillar-0	GAP baseline	0.8003	0.5980	0.5972	0.6923
	Mask-free attn pooling	0.8562	0.6925	0.6571	0.7437
	Support-masked pooling	0.8578	0.6884	0.6598	0.7424

5. Results

5.1. Support-masked pooling improves internal classification across encoder families

We first evaluated whether anatomy-aware support pooling improves study-level classification on the MERLIN internal test split. This experiment isolates the effect of the aggregation head by comparing three encoder-compatible pooling modes: GAP, mask-free attention pooling, and support-masked pooling while keeping the backbone family and end-to-end training protocol fixed.

Table 4 shows an encoder-dependent pattern. For DINOv3 and I3D-ResNet-121, support-masked pooling achieved the strongest overall performance. For DINOv3, macro-AUROC improved from 0.8380 with GAP to 0.8576 with support-masked pooling, while macro-AUPRC increased from 0.6382 to 0.6763. For I3D-ResNet-121, macro-AUROC increased from 0.8288 to 0.8482 and macro-AUPRC from 0.6169 to 0.6587. These gains indicate that, for a generic pretrained transformer and a native 3D convolutional encoder, study-level performance is limited not only by local feature quality but also by how spatial evidence is aggregated.

Pillar-0 exhibited a different profile. Replacing GAP with mask-free attention pooling produced the dominant improvement, increasing macro-AUROC from 0.8003 to 0.8562 and macro-AUPRC from 0.5980 to 0.6925. Support-masked pooling yielded a similar macro-AUROC of 0.8578, with a smaller and metric-dependent incremental benefit over mask-free attention.

Figure 4 provides a disease-level view of the same pattern. For DINOv3 and I3D-ResNet-121, support-masked pooling produced broader positive Δ AUROC shifts relative to GAP than mask-free attention pooling. In contrast, Pillar-0 showed a smaller additional gain from support masking after learned attention was introduced. Together, these results suggest that explicit anatomical support restriction is most beneficial when anatomical structure is not already strongly represented by the backbone. Full 95% bootstrap confidence intervals for all metrics are provided in Supplementary Table S1.

5.2. Support-masked pooling improves frozen external transfer

We next evaluated whether the internal gains persisted under frozen external transfer. All models were trained on MERLIN, and model selection, calibration parameters, and operating thresholds were selected on MERLIN validation and transferred unchanged to Duke-Abdomen and AMOS.

On the harmonized 10-label subset shared across MERLIN, Duke-Abdomen, and AMOS, support-masked pooling achieved the highest macro-AUROC across all three encoder families (Table 5). For DINOv3, support-masked pooling improved AUROC from 0.8022 to 0.8353 on Duke-Abdomen and from 0.7424 to 0.7616 on AMOS relative to GAP. AUPRC increased from 0.6276 to 0.6828 on Duke-Abdomen and from 0.3125 to 0.3502 on AMOS. For I3D-ResNet-121, AUROC improved from 0.7751 to 0.8197 on Duke-Abdomen and from 0.7135 to 0.7345 on AMOS, with corresponding AUPRC gains from 0.5903 to 0.6461 and from 0.2936 to 0.3273.

Table 5

External abdomen generalization on the harmonized 10-label subset across encoder families. Performance on the 10 findings shared across MERLIN, Duke–Abdomen, and AMOS. We compare the GAP baseline, mask-free attention pooling, and support-masked pooling. Metrics are macro-averaged over the harmonized label set. Pillar–0 is included for contextual comparison (see 4.4). Point estimates are shown for readability. Full 95% bootstrap confidence intervals for all metrics are provided in Supplementary Table S2.

Backbone	Mode	MERLIN		Duke		AMOS	
		AUROC	AUPRC	AUROC	AUPRC	AUROC	AUPRC
DINOv3	GAP baseline	0.8405	0.6727	0.8022	0.6276	0.7424	0.3125
	Mask-free attn pooling	0.8461	0.6963	0.8131	0.6494	0.7401	0.3214
	Support-masked pooling	0.8583	0.7042	0.8353	0.6828	0.7616	0.3502
I3D–ResNet-121	GAP baseline	0.8238	0.6411	0.7751	0.5903	0.7135	0.2936
	Mask-free attn pooling	0.8064	0.6370	0.7700	0.5740	0.7141	0.2905
	Support-masked pooling	0.8468	0.6705	0.8197	0.6461	0.7345	0.3273
Pillar–0	GAP baseline	0.7999	0.6517	0.7818	0.5781	0.7137	0.2850
	Mask-free attn pooling	0.8630	0.7458	0.8488	0.7034	0.7570	0.3928
	Support-masked pooling	0.8854	0.7448	0.8538	0.7032	0.7714	0.4022

Table 6

MERLIN-to-Duke transfer on the shared 27-label Abdominal CT subset. Performance is reported on the 27 findings shared between MERLIN and Duke–Abdomen. Pillar–0 is included for contextual cross-encoder comparison (see 4.4). Full 95% bootstrap confidence intervals for Duke–Abdomen are provided in Supplementary Table S3.

Backbone	Mode	MERLIN (27-label subset)				Duke–Abdomen (27-label subset)			
		AUROC	AUPRC	F1	BA	AUROC	AUPRC	F1	BA
DINOv3	GAP baseline	0.8368	0.6344	0.6345	0.7274	0.8212	0.6460	0.6194	0.7151
	Mask-free attn pooling	0.8466	0.6599	0.6441	0.7257	0.8312	0.6709	0.6134	0.7229
	Support-masked pooling	0.8582	0.6771	0.6610	0.7460	0.8483	0.6988	0.6335	0.7375
I3D–ResNet-121	GAP baseline	0.8269	0.6126	0.6091	0.7098	0.7911	0.6143	0.5964	0.6875
	Mask-free attn pooling	0.8165	0.6043	0.6029	0.7086	0.7933	0.6083	0.5888	0.7037
	Support-masked pooling	0.8471	0.6561	0.6422	0.7417	0.8280	0.6622	0.6269	0.7346
Pillar–0	GAP baseline	0.7968	0.5902	0.5911	0.6880	0.7750	0.5940	0.5500	0.6680
	Mask-free attn pooling	0.8544	0.6894	0.6530	0.7393	0.8280	0.6820	0.6240	0.7210
	Support-masked pooling	0.8572	0.6867	0.6564	0.7386	0.8330	0.6930	0.6170	0.7160

For Pillar–0, the encoder-dependent pattern observed internally persisted under transfer: on Duke–Abdomen, mask-free attention improved AUROC from 0.7818 to 0.8488, and support-masked pooling further increased AUROC to 0.8538. On AMOS, the corresponding values were 0.7137, 0.7570, and 0.7714.

Figure 5 summarizes the harmonized external-transfer results. At the dataset level, support-masked pooling remained the strongest AUROC setting across backbones, while all methods showed a larger performance drop on AMOS than on Duke–Abdomen. At the disease level, the Duke-to-AMOS degradation was not uniform across labels; instead, a subset of findings accounted for a disproportionate share of the macro-AUROC reduction. Thus, the lower AMOS performance reflects not only broad dataset shift but also disease-specific differences in detectability, label definition, or case mix. Full 95% bootstrap confidence intervals for the harmonized 10-label evaluation are reported in Supplementary Table S2.

5.3. Disease-level Duke–Abdomen transfer gains are broadly distributed but support-dependent

The harmonized 10-label analysis provides the cleanest three-dataset comparison, but it does not capture the full Duke–Abdomen label overlap. We therefore additionally evaluated MERLIN-to-Duke transfer on the broader 27-label subset shared between MERLIN and Duke–Abdomen. At the dataset level, support-masked pooling remained the

strongest or near-strongest setting across encoder families (Table 6); full 95% bootstrap confidence intervals for this Duke shared-27 evaluation are provided in Supplementary Table S3. To determine whether these dataset-level gains were driven by a few labels or distributed across the broader Duke label space, we examined per-finding Δ AUROC relative to GAP (Figure 6). Full absolute per-disease AUROC values for the Duke shared-27 evaluation are provided in Supplementary Figure S1.

The heatmap shows that support-masked pooling produced broadly positive shifts across many Duke labels, particularly for anatomically localized or measurement-linked findings. Large and consistent gains were observed for hydronephrosis, prostatomegaly, hepatic steatosis, abdominal aortic aneurysm, renal cysts, biliary ductal dilation, cardiomegaly, and pancreatic atrophy. For example, hydronephrosis improved by +0.13, +0.24, and +0.30 AUROC for DINOv3, I3D-ResNet-121, and Pillar-0, respectively. These disease-level patterns support the central hypothesis that label-specific anatomical support provides useful inductive bias when the spatial distribution of diagnostic evidence is well matched to the assigned support.

The heatmap also shows that support-masked pooling is not uniformly beneficial for every finding. Negative or minimal deltas were observed for a smaller subset of labels, including appendicitis, free air, thrombosis, and lymphadenopathy. These cases likely reflect different failure modes. For appendicitis, the localized appendix-focused support may be too narrow or sensitive to segmentation and downsampling errors. In contrast, thrombosis, free air, ascites, anasarca, metastatic disease, and lymphadenopathy were assigned global support because their evidence can be distributed, sparse, or anatomically variable; for these labels, support-masked pooling provides limited additional anatomical restriction beyond the full-lattice attention pathway. Several of these labels also have low positive prevalence and/or incomplete annotation in MERLIN, which can increase the variance of per-finding transfer estimates (Supplementary Figure S2). Thus, disease-level gains depend on both support suitability and the amount and quality of label supervision.

5.4. Support-masked attention provides auditable anatomical evidence aggregation

Finally, we examined whether support-masked attention weights could be used to audit the anatomical support from which study-level evidence was aggregated. Figure 7 shows representative examples for pleural effusion, hepatic steatosis, renal cyst, and pancreatic atrophy, including true-positive cases from DINOv3 support-masked and Pillar-0 support-masked models, as well as representative false-positive cases from DINOv3 support-masked models.

Across true-positive examples, high-response regions remained confined to the predefined anatomical support for the corresponding label. For pleural effusion, attention was restricted to the lung and pleural-context support; for hepatic steatosis, responses were constrained to the comparative liver-spleen support; for renal cyst, attention remained within kidney-centered support; and for pancreatic atrophy, responses were confined to the pancreatic support. This pattern was observed for both the generic pretrained DINOv3 encoder and the radiology-native Pillar-0 encoder, suggesting that support-masked pooling enforces a similar anatomy-constrained evidence pathway despite substantial differences in backbone pretraining and feature representation.

The false-positive examples provide a complementary audit. Although the predicted labels were incorrect, the attention responses generally remained within the assigned anatomical support rather than drifting toward unrelated organs or background anatomy. These cases therefore suggest that some ORACLE-CT errors can occur despite anatomically plausible support localization, reflecting limitations of study-level supervision, label noise, visual ambiguity, or insufficient discriminative evidence within the correct support region rather than gross off-target aggregation.

These maps should be interpreted as qualitative audits of the aggregation support, not as definitive lesion-level explanations. Because voxel or lesion-level ground truth was unavailable for most findings, the overlays cannot prove that the classifier attended to the causal abnormality. Rather, they verify an important property of the proposed head: the evidence used for study-level pooling is constrained to the anatomical support assigned to each label.

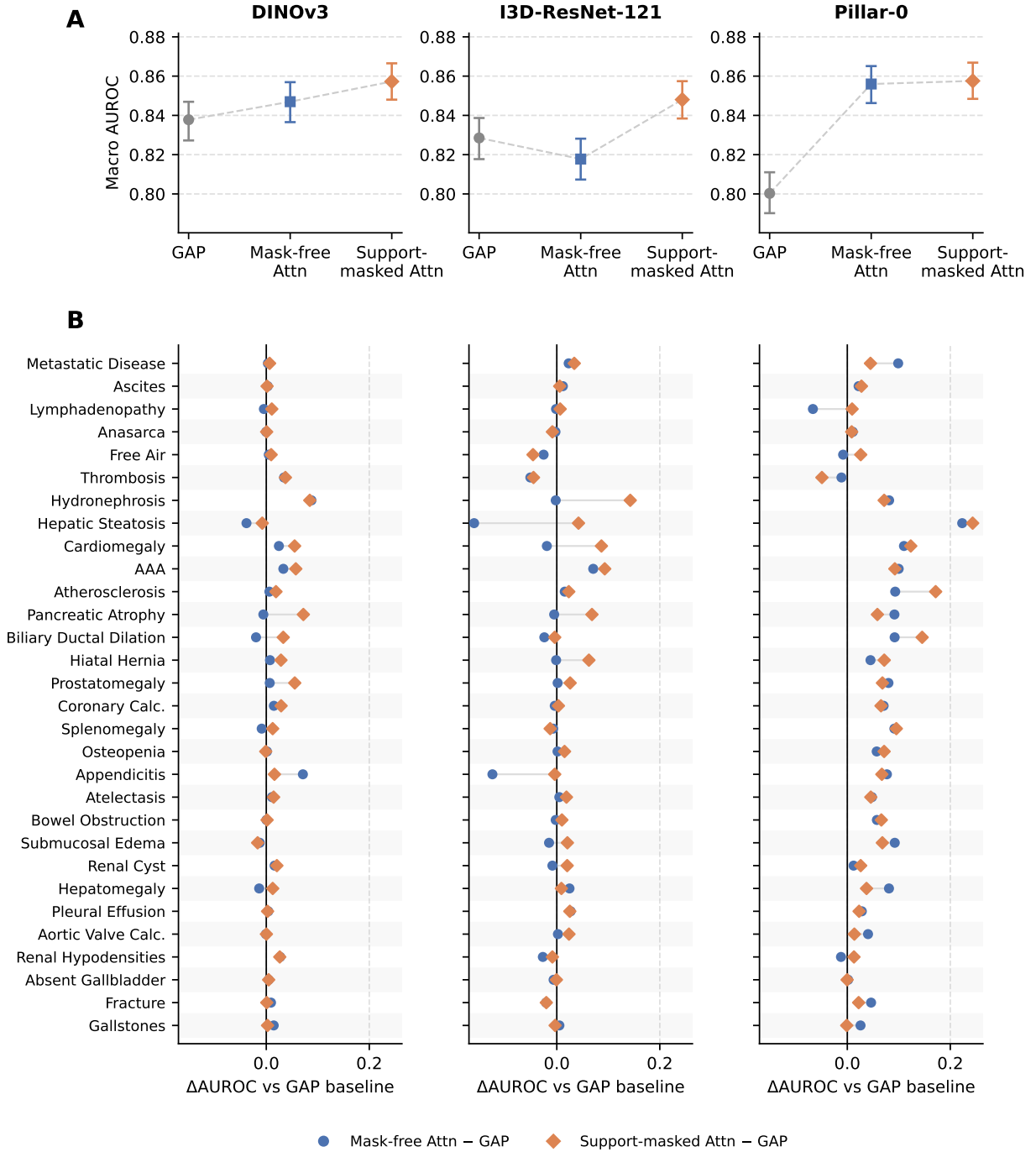


Figure 4: ORACLE-CT: Encoder-dependent internal test results on MERLIN (n=5,082). (A) Macro-averaged AUROC on the MERLIN test set across three pooling modes for each encoder backbone. Error bars denote 95% bootstrap confidence intervals (1,000 bootstrap replicates). (B) Per-disease Δ AUROC relative to the GAP baseline for mask-free attention pooling (blue circles) and support-masked attention pooling (orange diamonds). Diseases are ordered by the average support-masked Δ AUROC gain over GAP across the three backbones (ascending from bottom to top). For DINOv3 and I3D-ResNet-121, support-masked pooling yields broader positive disease-level shifts and the strongest dataset-level AUROC, whereas for Pillar-0 the dominant gain arises from replacing GAP with learned attention, with support masking providing a smaller additional benefit.

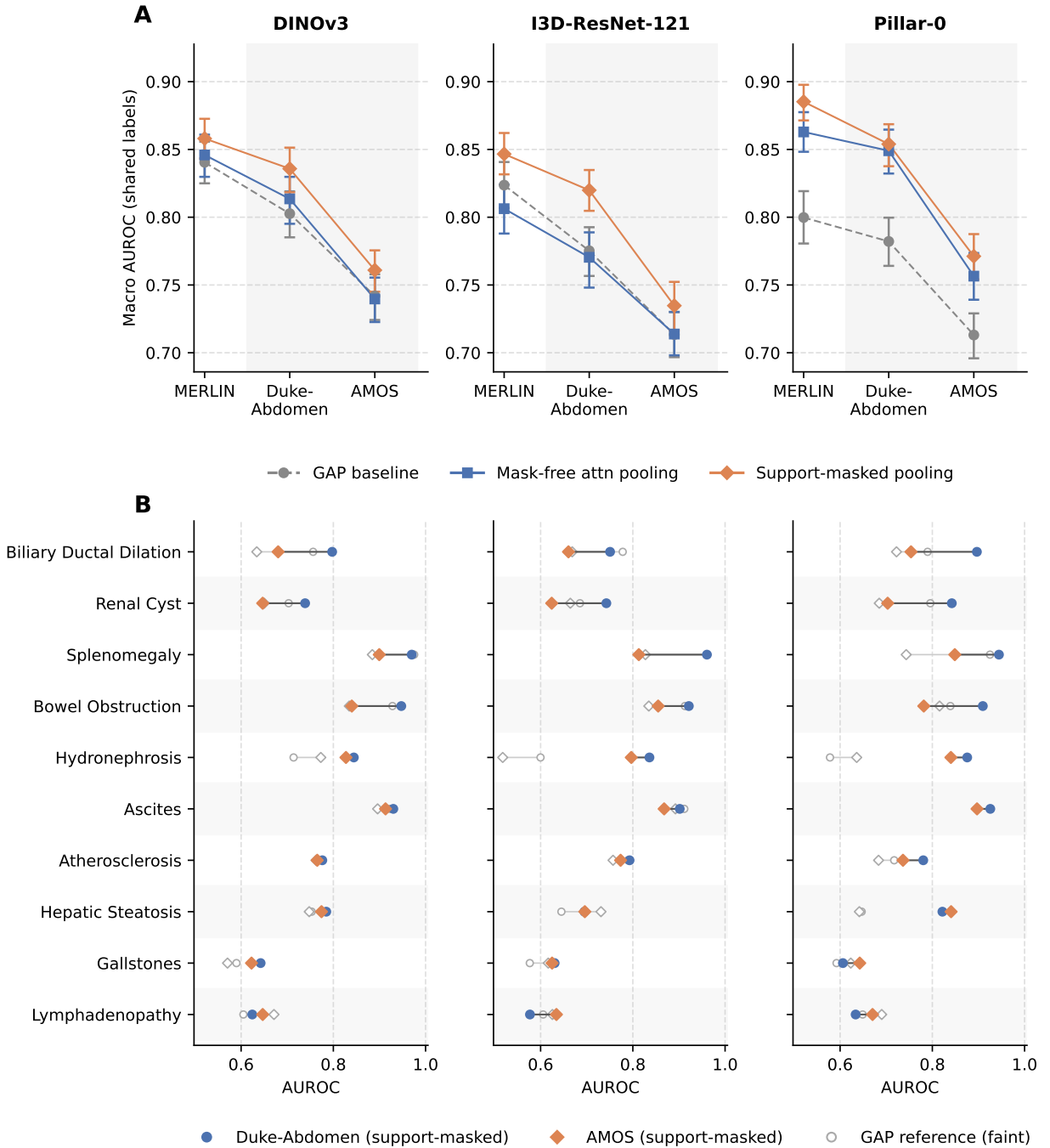


Figure 5: External generalization on the harmonized 10-label subset. (A) Macro AUROC across MERLIN, Duke-Abdomen, and AMOS for GAP, mask-free attention pooling, and support-masked pooling across DINOv3, I3D-ResNet-121, and Pillar-0. Error bars denote 95% bootstrap confidence intervals. (B) Disease-level decomposition of the Duke-to-AMOS shift for the support-masked model on the 10 harmonized labels. Blue circles denote Duke AUROC and orange diamonds denote AMOS AUROC, with horizontal black segments connecting the same disease across datasets; longer leftward shifts indicate larger degradation on AMOS. Hollow gray markers show the corresponding GAP baseline values as a faint reference. Diseases are ordered by average Duke-to-AMOS AUROC change under support-masked pooling across backbones. While support-masked pooling remains the strongest dataset-level transfer setting in Panel A, Panel B shows that the AMOS performance drop is not uniform across labels, but is disproportionately driven by a subset of harmonized findings.

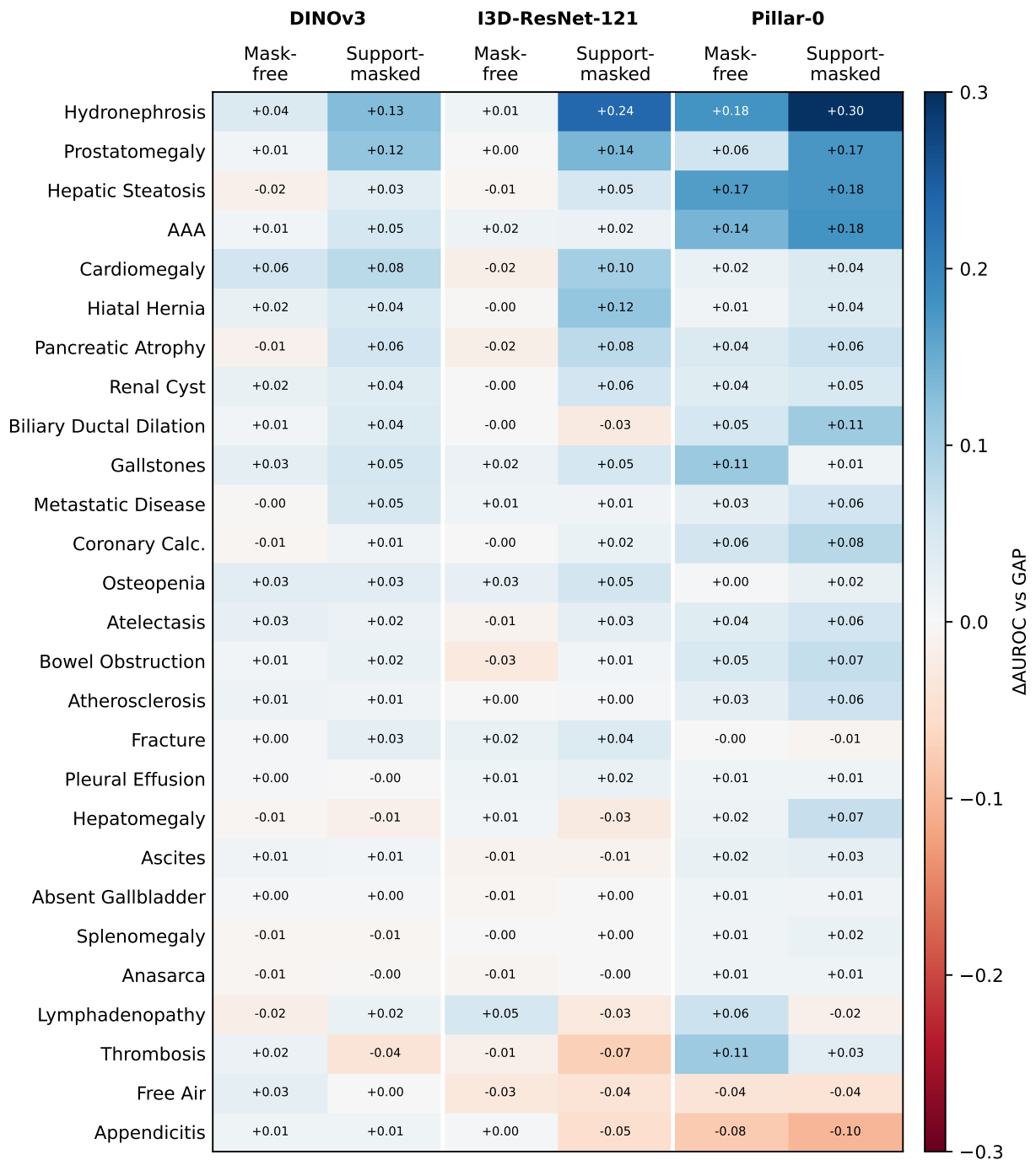


Figure 6: Disease-level MERLIN-to-Duke transfer on the shared 27-label subset. Heatmap of per-finding Δ AUROC relative to GAP on Duke–Abdomen for mask-free attention pooling and support-masked pooling across DINOv3, I3D–ResNet-121, and Pillar-0. Blue indicates improvement over uniform full-lattice aggregation, red indicates lower AUROC than GAP, and values denote absolute AUROC differences. Rows are ordered by the average support-masked gain across encoders. Support-masked pooling produces broadly distributed gains for many anatomically localized or measurement-linked findings, whereas smaller or negative deltas occur for labels with sparse or variable evidence, low positive prevalence, incomplete annotation, or intentionally global support definitions where support-masked pooling reduces to full-lattice attention and therefore provides limited additional anatomical constraint. Full absolute per-disease AUROC values are provided in Supplementary Figure S1.

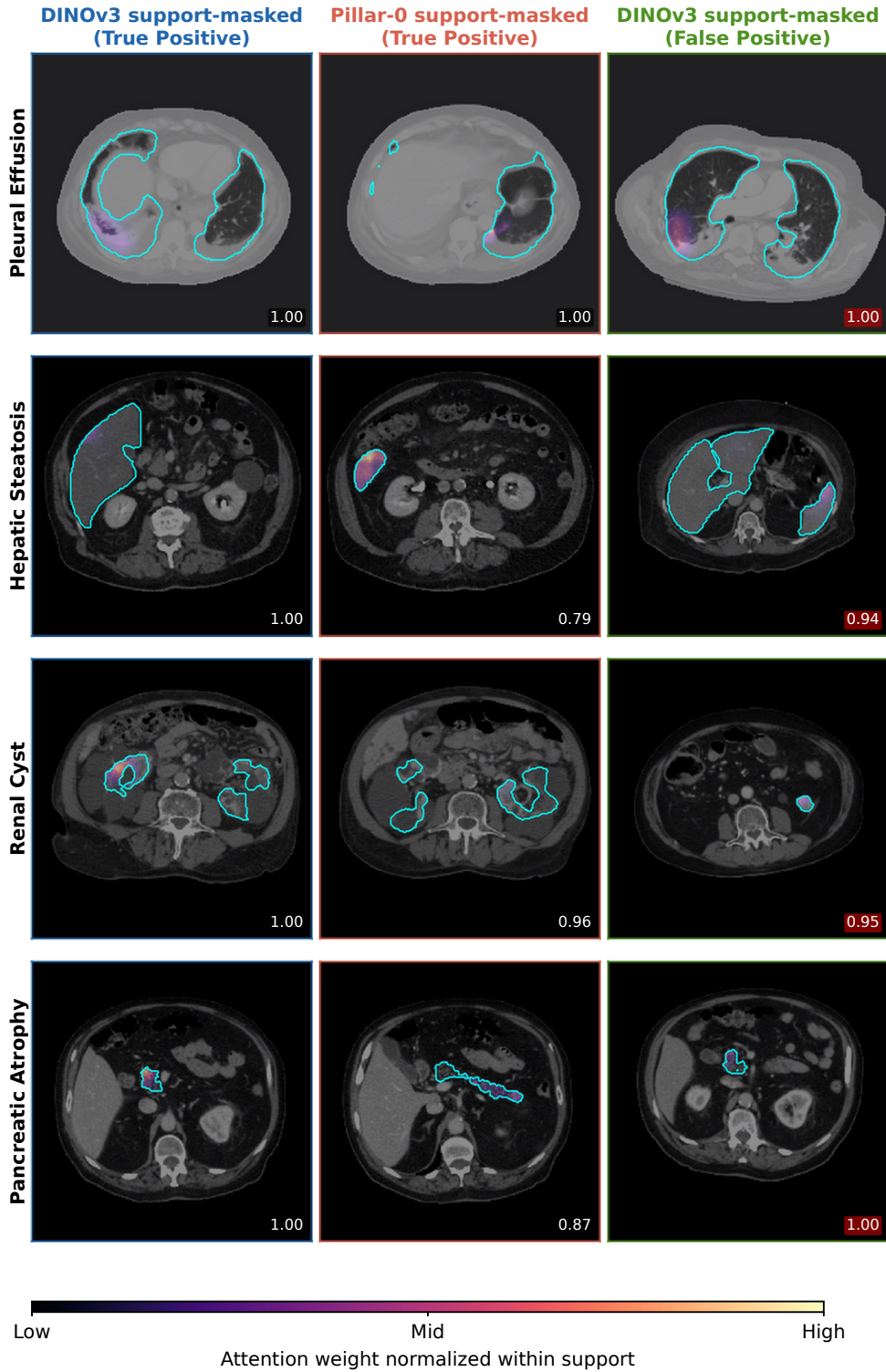


Figure 7: Qualitative audit of support-masked attention. Representative axial CT slices with anatomical support contours and support-masked attention overlays for pleural effusion, hepatic steatosis, renal cyst, and pancreatic atrophy. Columns show true-positive examples from DINOv3 support-masked and Pillar-0 support-masked models, and representative false-positive examples from DINOv3 support-masked models. Attention remains concentrated within the assigned anatomical support in both true-positive and false-positive examples, indicating that ORACLE-CT errors can occur despite anatomically plausible support localization. Score badges denote sigmoid output for the positive class.

6. Discussion

This study investigated whether multi-label abdominal CT classification benefits from making the aggregation stage explicitly anatomy-aware. Across internal and frozen external evaluation, replacing unrestricted full-lattice aggregation with label-specific support pooling improved performance most clearly for DINOv3 and I3D-ResNet-121. These gains indicate that, even with strong pretrained encoders, the way spatial evidence is summarized into finding-level predictions can substantially affect discrimination and transfer.

The benefit of support-masked pooling can be understood as a constraint on the spatial competition induced by attention pooling. Global average pooling compresses features without regard to anatomical compartment, while mask-free attention learns non-uniform weights but still normalizes over the full feature lattice. Support-masked pooling changes this normalization domain: evidence competes only within the anatomical support assigned to each label. This distinction was especially important for I3D-ResNet-121, where mask-free attention slightly underperformed GAP. A plausible explanation is that the native 3D CNN lattice is highly downsampled and locally smoothed, so an unconstrained unary attention head must learn both content weighting and anatomical localization from study-level labels alone. In that setting, attention may overemphasize non-specific high-response locations, producing a less stable summary than uniform averaging. Anatomical support restriction acts as a regularizer by converting attention from an unconstrained localization problem into a within-support evidence aggregation problem.

The Pillar-0 results refine this interpretation. For this radiology-native foundation encoder, most of the gain came from replacing GAP with learned attention, while explicit support masking produced a smaller and metric-dependent incremental benefit. This pattern suggests that radiology-specific pretraining may already encode part of the spatial and anatomical organization that ORACLE-CT introduces explicitly at pooling time. However, the masking benefit did not disappear, particularly for AUROC under external transfer, indicating that explicit anatomical support and radiology-native representation learning are partially complementary. In practice, support masking appears most valuable when anatomical priors are weak in the encoder, but it can still provide structure and auditability when stronger medical pretraining is available.

The disease-level analyses show that the value of anatomy-aware aggregation is support-dependent. Gains were largest for findings whose diagnostic evidence is anatomically localized. In contrast, smaller or negative deltas occurred for labels whose assigned support was either difficult to define precisely or intentionally global. Appendicitis may be sensitive to a narrow appendix-focused proxy and to segmentation or downsampling errors, whereas thrombosis, free air, ascites, anasarca, metastatic disease, and lymphadenopathy were assigned global support because their evidence can be sparse, distributed, or anatomically variable. For such labels, support-masked pooling provides limited additional restriction beyond full-lattice attention. Several of these findings also have low positive prevalence or incomplete annotation in MERLIN, which can make disease-level estimates less stable.

The same analysis also highlights a limit of fixed support design. Not all findings are intrinsic to a single organ; some depend on a broader reference frame. Hepatomegaly is the clearest example - liver size is interpreted relative to patient body habitus, and recent habitus-aware abdominal anatomy generation work similarly models organ size as a residual relative to body scale rather than as an isolated volume [4]. A strictly single-organ support is therefore under-specified for size-against-reference findings, which may partly explain the inconsistent gains observed for hepatomegaly across encoders, with a clear improvement appearing only for Pillar-0, whose pretraining likely encodes body-scale context independently.

Several limitations should be acknowledged. First, ORACLE-CT depends on upstream segmentation and can inherit failures from missing, truncated, or inaccurate masks. Although support dilation and fallback handling reduce some practical failure modes, the sensitivity of support-masked pooling to segmentation quality, support size, and encoder-lattice resolution should be quantified more systematically. Second, the label-to-support mapping was manually specified from clinical anatomy and fixed across datasets. This improves interpretability and enables frozen external evaluation, but may be suboptimal for findings with variable, multi-compartment, or weakly localized evidence. Third, labels were examination-level and report-derived, and may contain structured missingness, incomplete co-labeling, and dataset-specific reporting patterns; these issues are especially relevant for rare findings or clinically correlated labels, where models may learn associations that are valid in one dataset but less stable externally. Finally, this study focused on abdominal CT and a single-volume classification setting, and therefore did not address other body regions, lesion-level tasks, multi-series examinations, contrast-phase integration, or longitudinal patient-level modeling.

These limitations suggest several future directions. One direction is to reduce dependence on a separate segmentation pipeline by developing hybrid models that jointly learn anatomical localization and multi-label classification, or that propagate uncertainty from anatomical support maps into the classification head. A second direction is to make support definitions more adaptive: instead of using fixed label-to-support assignments, future models could learn support mixtures, conditionally expand or contract supports, or refine coarse anatomical priors while preserving auditability. Finally, extending anatomy-aware aggregation to multi-series, multi-phase, and longitudinal CT interpretation would better reflect clinical radiology workflows, where decisions often depend on contrast phase, reconstruction type, and comparison with prior examinations. Such extensions will require datasets with more consistently curated cross-series and temporal supervision than is currently available in most large-scale abdominal CT benchmarks.

7. Conclusion

We presented ORACLE-CT, an anatomy-aware support-pooling framework for multi-label abdominal CT classification. ORACLE-CT assigns each finding to a predefined anatomical support derived from multi-organ segmentation and restricts evidence aggregation to that support, without changing the encoder architecture or training protocol. Across DINOv3, I3D-ResNet-121, and Pillar-0, the results show that where spatial evidence is aggregated is a major design choice in volumetric CT classification. Support-masked pooling provided the clearest gains for DINOv3 and I3D-ResNet-121, whereas Pillar-0 showed smaller and metric-dependent benefit beyond learned attention, suggesting that radiology-native pretraining may reduce, but not eliminate, the value of explicit anatomical support. Overall, ORACLE-CT provides a practical encoder-agnostic mechanism for making CT classifiers more anatomically aligned, externally robust, and auditable at the evidence-aggregation stage.

Code, Model and Data Availability

Code and trained model weights for ORACLE-CT will be made available at public repository upon publication. MERLIN and AMOS are public datasets available from their respective dataset/challenge sources. Duke-Abdomen is a private institutional dataset and cannot be publicly released because of institutional and patient-privacy restrictions.

Acknowledgements

Some schematic icons used in Figure 2 and Graphical Abstract were adapted from Servier Medical Art (<https://smart.servier.com/>), licensed under CC BY 4.0 (<https://creativecommons.org/licenses/by/4.0/>), and from Flaticon (<https://www.flaticon.com/>), used according to the respective source licenses. This work was funded by the Center for Virtual Imaging Trials, NIH grants P41EB028744, R01EB001838, and R01CA261457.

References

- [1] Agrawal, K.K., Liu, L., Lian, L., Nercessian, M., Harguindeguy, N., Wu, Y., Mikhael, P., Lin, G., Sequist, L.V., Fintelmann, F., et al., 2025. Pillar-0: A new frontier for radiology foundation models. arXiv preprint arXiv:2511.17803 .
- [2] Bahdanau, D., Cho, K., Bengio, Y., 2014. Neural machine translation by jointly learning to align and translate. arXiv preprint arXiv:1409.0473 .
- [3] Beeche, C., Kim, J., Tavolinejad, H., Zhao, B., Sharma, R., Duda, J., Gee, J., Dako, F., Verma, A., Morse, C., et al., 2025. A pan-organ vision-language model for generalizable 3d ct representations. medRxiv .
- [4] Bhandari, Y., Dahal, L., Segars, P., Lo, J.Y., 2026. Abdomengen: Sequential volume-conditioned diffusion framework for abdominal anatomy generation. arXiv preprint arXiv:2604.12969 .
- [5] Blankemeier, L., Cohen, J.P., Kumar, A., Van Veen, D., Gardezi, S.J.S., Paschali, M., Chen, Z., Delbrouck, J.B., Reis, E., Truys, C., et al., 2024. Merlin: A vision language foundation model for 3d computed tomography. Research Square , rs-3.
- [6] Carreira, J., Zisserman, A., 2017. Quo vadis, action recognition? a new model and the kinetics dataset, in: proceedings of the IEEE Conference on Computer Vision and Pattern Recognition, pp. 6299-6308.
- [7] Cho, J.H., Kim, S.S., 2020. Peritoneal carcinomatosis and its mimics: review of ct findings for differential diagnosis. Journal of the Belgian Society of Radiology 104, 8.
- [8] CodaBench, 2026. Foundation models for general ct image diagnosis challenge Accessed: 2026-05-02.
- [9] Dahal, L., Ghoghnejad, M., Vancouillie, L., Ghosh, D., Bhandari, Y., Kim, D., Ho, F.C., Tushar, F.I., Luo, S., Lafata, K.J., et al., 2025. Xcat 3.0: A comprehensive library of personalized digital twins derived from ct scans. Medical Image Analysis , 103636.
- [10] Dieterich, T.G., Lathrop, R.H., Lozano-Pérez, T., 1997. Solving the multiple instance problem with axis-parallel rectangles. Artificial intelligence 89, 31-71.

- [11] Dosovitskiy, A., Beyer, L., Kolesnikov, A., Weissenborn, D., Zhai, X., Unterthiner, T., Dehghani, M., Minderer, M., Heigold, G., Gelly, S., et al., 2020. An image is worth 16x16 words: Transformers for image recognition at scale. arXiv preprint arXiv:2010.11929 .
- [12] Draelos, R.L., Dov, D., Mazurowski, M.A., Lo, J.Y., Henao, R., Rubin, G.D., Carin, L., 2021. Machine-learning-based multiple abnormality prediction with large-scale chest computed tomography volumes. *Medical image analysis* 67, 101857.
- [13] Garcia-Alcoser, M.E., GhoghjNejad, M., Tushar, F.I., Kim, D., Lafata, K.J., Rubin, G.D., Lo, J.Y., 2025. Evaluating large language models for zero-shot disease labeling in ct radiology reports across organ systems. arXiv preprint arXiv:2506.03259 .
- [14] Haghshomar, M., Antonacci, D., Smith, A.D., Thaker, S., Miller, F.H., Borhani, A.A., 2024. Diagnostic accuracy of ct for the detection of hepatic steatosis: a systematic review and meta-analysis. *Radiology* 313, e241171.
- [15] Hamamci, I.E., Er, S., Wang, C., Almas, F., Simsek, A.G., Esirgun, S.N., Doga, I., Durugol, O.F., Dai, W., Xu, M., et al., 2024. Developing generalist foundation models from a multimodal dataset for 3d computed tomography. arXiv preprint arXiv:2403.17834 .
- [16] He, K., Zhang, X., Ren, S., Sun, J., 2016. Deep residual learning for image recognition, in: *Proceedings of the IEEE conference on computer vision and pattern recognition*, pp. 770–778.
- [17] Hu, Y., Luo, X., Wang, Z., Li, D., Qiu, L., . Segmentation helps understanding: Mask-infused vision-language pre-training for 3d medical images .
- [18] Ilse, M., Tomczak, J., Welling, M., 2018. Attention-based deep multiple instance learning, in: *International conference on machine learning*, PMLR. pp. 2127–2136.
- [19] Le Guellec, B., Lefèvre, A., Geay, C., Shorten, L., Bruge, C., Hacein-Bey, L., Amouyel, P., Pruvo, J.P., Kuchcinski, G., Hamroun, A., 2024. Performance of an open-source large language model in extracting information from free-text radiology reports. *Radiology: Artificial Intelligence* 6, e230364.
- [20] Lee, H.C., Liu, Z., Ahmed, H., Kim, S., Huver, S., Nath, V., Fayad, Z.A., Deyer, T., Mei, X., 2025. Unified supervision for vision-language modeling in 3d computed tomography. arXiv preprint arXiv:2509.01554 .
- [21] Li, Y., Ming, S., Zhao, M., Lai, H., Wang, R., Zhou, R., Wang, R., Li, Y., Wei, W., Zhou, S.K., 2026. Greenfm: Toward a resource-efficient radiology foundation model. arXiv preprint arXiv:2603.06467 .
- [22] Lin, J., Xia, Y., Zhang, J., Yan, K., Lu, L., Luo, J., Zhang, L., 2024. Ct-glip: 3d grounded language-image pretraining with ct scans and radiology reports for full-body scenarios. arXiv preprint arXiv:2404.15272 .
- [23] Lin, M., Chen, Q., Yan, S., 2013. Network in network. arXiv preprint arXiv:1312.4400 .
- [24] Liu, C., Chen, Y., Shi, H., Lu, J., Jian, B., Pan, J., Cai, L., Wang, J., Zhang, Y., Li, J., et al., 2025. Does dinov3 set a new medical vision standard? arXiv preprint arXiv:2509.06467 .
- [25] Luong, M.T., Pham, H., Manning, C.D., 2015. Effective approaches to attention-based neural machine translation. arXiv preprint arXiv:1508.04025 .
- [26] MEYERS, M.A., 1973. Distribution of intra-abdominal malignant seeding: dependency on dynamics of flow of ascitic fluid. *American Journal of Roentgenology* 119, 198–206.
- [27] Mukherjee, P., Hou, B., Lanfredi, R.B., Summers, R.M., 2023. Feasibility of using the privacy-preserving large language model vicuna for labeling radiology reports. *Radiology* 309, e231147.
- [28] Organisation for Economic Co-operation and Development, 2025. Computed tomography (ct) exams URL: <https://www.oecd.org/en/data/indicators/computed-tomography-ct-exams.html>. accessed: 2025-10-29.
- [29] Pickhardt, P.J., Blake, G.M., Moeller, A., Garrett, J.W., Summers, R.M., 2024. Post-contrast ct liver attenuation alone is superior to the liver-spleen difference for identifying moderate hepatic steatosis. *European Radiology* 34, 7041–7052.
- [30] Pourvaziri, A., Narayan, A.K., Tso, D., Baliyan, V., Glover IV, M., Bizzo, B.C., Kako, B., Succì, M.D., Lev, M.H., Flores, E.J., 2022. Imaging information overload: Quantifying the burden of interpretive and non-interpretive tasks for computed tomography angiography for aortic pathologies in emergency radiology. *Current Problems in Diagnostic Radiology* 51, 546–551.
- [31] Radford, A., Kim, J.W., Hallacy, C., Ramesh, A., Goh, G., Agarwal, S., Sastry, G., Askell, A., Mishkin, P., Clark, J., et al., 2021. Learning transferable visual models from natural language supervision, in: *International conference on machine learning*, PmLR. pp. 8748–8763.
- [32] Reichenpfader, D., Müller, H., Denecke, K., 2024. A scoping review of large language model based approaches for information extraction from radiology reports. *npj Digital Medicine* 7, 222.
- [33] Sellergren, A., Kazemzadeh, S., Jaroensri, T., Kiraly, A., Traverse, M., Kohlberger, T., Xu, S., Jamil, F., Hughes, C., Lau, C., et al., 2025. Medgemma technical report. arXiv preprint arXiv:2507.05201 .
- [34] Shui, Z., Zhang, J., Cao, W., Wang, S., Guo, R., Lu, L., Yang, L., Ye, X., Liang, T., Zhang, Q., et al., 2025. Large-scale and fine-grained vision-language pre-training for enhanced ct image understanding. arXiv preprint arXiv:2501.14548 .
- [35] Siemens Healthineers, . syngo.via — get the full picture. URL: <https://www.siemens-healthineers.com/en-us/molecular-imaging/pet-ct/syngo-via>. siemens Healthineers USA.
- [36] Silverman, S.G., Pedrosa, I., Ellis, J.H., Hindman, N.M., Schieda, N., Smith, A.D., Remer, E.M., Shinagare, A.B., Curci, N.E., Raman, S.S., et al., 2019. Bosniak classification of cystic renal masses, version 2019: an update proposal and needs assessment. *Radiology* 292, 475–488.
- [37] Siméoni, O., Vo, H.V., Seitzer, M., Baldassarre, F., Oquab, M., Jose, C., Khalidov, V., Szafraniec, M., Yi, S., Ramamonjisoa, M., et al., 2025. Dinov3. arXiv preprint arXiv:2508.10104 .
- [38] Smith-Bindman, R., Chu, P.W., Firdaus, H.A., Stewart, C., Malekheaday, M., Alber, S., Bolch, W.E., Mahendra, M., de González, A.B., Miglioretti, D.L., 2025. Projected lifetime cancer risks from current computed tomography imaging. *JAMA internal medicine* 185, 710–719.
- [39] Synopsys, . Simpleware auto segmentation tools. URL: <https://www.synopsys.com/simpleware/software/auto-segmentation.html>. synopsys Simpleware.
- [40] Tushar, F.I., D’Annibale, V.M., Hou, R., Mazurowski, M.A., Fu, W., Samei, E., Rubin, G.D., Lo, J.Y., 2021. Classification of multiple diseases on body ct scans using weakly supervised deep learning. *Radiology: Artificial Intelligence* 4, e210026.
- [41] Vaswani, A., Shazeer, N., Parmar, N., Uszkoreit, J., Jones, L., Gomez, A.N., Kaiser, Ł., Polosukhin, I., 2017. Attention is all you need. *Advances in neural information processing systems* 30.

- [42] Vosshenrich, J., Brantner, P., Cyriac, J., Boll, D.T., Merkle, E.M., Heye, T., 2021. Quantifying radiology resident fatigue: analysis of preliminary reports. *Radiology* 298, 632–639.
- [43] Wald, T., Hamamci, I.E., Gao, Y., Bond-Taylor, S., Sharma, H., Ilse, M., Lo, C., Melnichenko, O., Codella, N.C., Wetscherek, M.T., et al., 2025. Comprehensive language-image pre-training for 3d medical image understanding. *arXiv preprint arXiv:2510.15042* .
- [44] Wang, X., Girshick, R., Gupta, A., He, K., 2018. Non-local neural networks, in: *Proceedings of the IEEE conference on computer vision and pattern recognition*, pp. 7794–7803.
- [45] Wasserthal, J., Breit, H.C., Meyer, M.T., Pradella, M., Hinck, D., Sauter, A.W., Heye, T., Boll, D.T., Cyriac, J., Yang, S., et al., 2023. Totalsegmentator: robust segmentation of 104 anatomic structures in ct images. *Radiology: Artificial Intelligence* 5, e230024.
- [46] Xu, K., Ba, J., Kiros, R., Cho, K., Courville, A., Salakhudinov, R., Zemel, R., Bengio, Y., 2015. Show, attend and tell: Neural image caption generation with visual attention, in: *International conference on machine learning*, PMLR, pp. 2048–2057.
- [47] Yang, A., Li, A., Yang, B., Zhang, B., Hui, B., Zheng, B., Yu, B., Gao, C., Huang, C., Lv, C., et al., 2025. Qwen3 technical report. *arXiv preprint arXiv:2505.09388* .
- [48] Zaheer, M., Kottur, S., Ravanbakhsh, S., Póczos, B., Salakhutdinov, R.R., Smola, A.J., 2017. Deep sets. *Advances in neural information processing systems* 30.

8. Supplementary Material

Table S7

MERLIN full 30-label performance with 95% bootstrap confidence intervals. Values are macro-averaged point estimates with 95% bootstrap confidence intervals in brackets. Metrics are computed over the full 30-label MERLIN test set. Aggregation modes are abbreviated as GAP, Mask-free attention pooling, and Support-masked pooling. Bold values indicate the best point estimate within each backbone block.

Backbone	Aggregation mode	AUROC	AUPRC	F1	BA
DINOv3	GAP baseline	0.838[0.827–0.847]	0.638[0.624–0.662]	0.636[0.618–0.650]	0.730[0.720–0.740]
	Mask-free	0.847[0.837–0.857]	0.662[0.647–0.683]	0.643[0.626–0.657]	0.726[0.717–0.736]
	Support-masked	0.858[0.848–0.867]	0.676[0.661–0.699]	0.660[0.643–0.673]	0.747[0.736–0.756]
I3D-ResNet-121	GAP baseline	0.829[0.818–0.839]	0.617[0.605–0.640]	0.611[0.593–0.624]	0.712[0.702–0.722]
	Mask-free	0.818[0.807–0.828]	0.609[0.595–0.631]	0.605[0.587–0.618]	0.710[0.700–0.720]
	Support-masked	0.848[0.838–0.857]	0.659[0.644–0.681]	0.642[0.626–0.655]	0.743[0.732–0.753]
Pillar-0	GAP baseline	0.800[0.790–0.811]	0.598[0.587–0.621]	0.597[0.580–0.612]	0.692[0.683–0.701]
	Mask-free	0.856[0.846–0.865]	0.693[0.680–0.711]	0.657[0.641–0.670]	0.744[0.734–0.753]
	Support-masked	0.858[0.848–0.867]	0.688[0.674–0.708]	0.660[0.644–0.672]	0.742[0.733–0.752]

Table S8

Harmonized 10-label performance with 95% bootstrap confidence intervals. Values are macro-averaged point estimates with 95% bootstrap confidence intervals in brackets. Metrics are computed over the 10-label subset shared across MERLIN, Duke-Abdomen, and AMOS. Models were trained on MERLIN; Duke-Abdomen and AMOS were used only for frozen external evaluation. Aggregation modes are abbreviated as GAP, Mask-free attention pooling, and Support-masked pooling. Bold values indicate the best point estimate within each cohort/backbone block.

Cohort	Backbone	Aggregation	AUROC	AUPRC	F1	BA
MERLIN	DINOv3	GAP	0.841[0.825–0.856]	0.673[0.648–0.704]	0.655[0.629–0.676]	0.694[0.678–0.710]
		Mask-free	0.846[0.830–0.861]	0.696[0.671–0.726]	0.670[0.645–0.693]	0.696[0.681–0.713]
		Support-masked	0.858[0.843–0.873]	0.704[0.680–0.736]	0.681[0.654–0.704]	0.712[0.694–0.729]
	I3D-ResNet-121	GAP	0.824[0.807–0.841]	0.641[0.619–0.673]	0.628[0.603–0.652]	0.680[0.664–0.696]
		Mask-free	0.806[0.788–0.824]	0.637[0.615–0.667]	0.625[0.602–0.647]	0.680[0.664–0.695]
		Support-masked	0.847[0.832–0.862]	0.670[0.648–0.702]	0.645[0.622–0.667]	0.704[0.686–0.722]
	Pillar-0	GAP	0.800[0.781–0.819]	0.652[0.629–0.684]	0.635[0.609–0.657]	0.672[0.658–0.687]
		Mask-free	0.863[0.848–0.877]	0.746[0.722–0.772]	0.698[0.674–0.718]	0.723[0.709–0.737]
		Support-masked	0.885[0.871–0.898]	0.745[0.720–0.772]	0.707[0.684–0.729]	0.729[0.714–0.744]
Duke-Abdomen	DINOv3	GAP	0.802[0.785–0.819]	0.628[0.603–0.659]	0.601[0.573–0.624]	0.662[0.640–0.685]
		Mask-free	0.813[0.795–0.830]	0.649[0.626–0.678]	0.625[0.599–0.647]	0.697[0.677–0.719]
		Support-masked	0.835[0.818–0.851]	0.683[0.659–0.714]	0.635[0.609–0.657]	0.701[0.678–0.723]
	I3D-ResNet-121	GAP	0.775[0.757–0.793]	0.590[0.568–0.623]	0.572[0.545–0.595]	0.641[0.621–0.662]
		Mask-free	0.770[0.748–0.789]	0.574[0.550–0.608]	0.558[0.531–0.583]	0.664[0.642–0.687]
		Support-masked	0.820[0.805–0.835]	0.646[0.622–0.676]	0.602[0.576–0.625]	0.701[0.678–0.725]
	Pillar-0	GAP	0.782[0.764–0.800]	0.578[0.556–0.610]	0.547[0.515–0.574]	0.637[0.621–0.652]
		Mask-free	0.849[0.832–0.865]	0.703[0.678–0.736]	0.651[0.622–0.674]	0.713[0.692–0.735]
		Support-masked	0.854[0.838–0.869]	0.703[0.678–0.734]	0.610[0.581–0.636]	0.693[0.671–0.714]
AMOS	DINOv3	GAP	0.742[0.724–0.758]	0.312[0.292–0.345]	0.297[0.274–0.320]	0.603[0.591–0.616]
		Mask-free	0.740[0.723–0.755]	0.321[0.300–0.355]	0.300[0.273–0.324]	0.613[0.599–0.626]
		Support-masked	0.762[0.745–0.776]	0.350[0.327–0.383]	0.350[0.324–0.371]	0.643[0.630–0.655]
	I3D-ResNet-121	GAP	0.714[0.697–0.730]	0.294[0.275–0.325]	0.267[0.244–0.290]	0.591[0.579–0.602]
		Mask-free	0.714[0.698–0.730]	0.291[0.271–0.321]	0.280[0.254–0.300]	0.616[0.604–0.628]
		Support-masked	0.735[0.716–0.752]	0.327[0.306–0.359]	0.306[0.282–0.327]	0.628[0.614–0.642]
	Pillar-0	GAP	0.714[0.696–0.729]	0.285[0.268–0.315]	0.250[0.225–0.273]	0.588[0.577–0.598]
		Mask-free	0.757[0.739–0.774]	0.393[0.368–0.424]	0.307[0.279–0.331]	0.605[0.593–0.617]
		Support-masked	0.771[0.754–0.788]	0.402[0.377–0.435]	0.287[0.261–0.311]	0.609[0.597–0.620]

Table S9

Duke–Abdomen shared 27-label performance with 95% bootstrap confidence intervals. Values are macro-averaged point estimates with 95% bootstrap confidence intervals in brackets. Models were trained on MERLIN, and Duke–Abdomen was used only for frozen external evaluation. Metrics are computed over the 27 labels shared between MERLIN and Duke–Abdomen. Aggregation modes are abbreviated as GAP, Mask-free attention pooling, and Support-masked pooling. Bold values indicate the best point estimate within each backbone block.

Backbone	Aggregation	AUROC	AUPRC	F1	BA
DINOv3	GAP	0.821[0.804–0.837]	0.646[0.631–0.673]	0.619[0.598–0.635]	0.715[0.700–0.729]
	Mask-free	0.831[0.816–0.845]	0.671[0.655–0.699]	0.613[0.592–0.631]	0.723[0.710–0.736]
	Support-masked	0.848[0.832–0.863]	0.699[0.684–0.726]	0.633[0.613–0.650]	0.737[0.722–0.752]
I3D–ResNet-121	GAP	0.791[0.773–0.809]	0.614[0.600–0.643]	0.596[0.576–0.613]	0.688[0.672–0.703]
	Mask-free	0.793[0.775–0.809]	0.608[0.594–0.636]	0.589[0.568–0.605]	0.704[0.687–0.720]
	Support-masked	0.828[0.813–0.842]	0.662[0.648–0.689]	0.627[0.607–0.642]	0.735[0.719–0.749]
Pillar-0	GAP	0.775[0.755–0.793]	0.594[0.579–0.622]	0.550[0.528–0.568]	0.668[0.654–0.682]
	Mask-free	0.828[0.811–0.843]	0.682[0.665–0.708]	0.624[0.603–0.642]	0.721[0.707–0.736]
	Support-masked	0.833[0.818–0.846]	0.693[0.678–0.718]	0.617[0.597–0.634]	0.716[0.703–0.729]

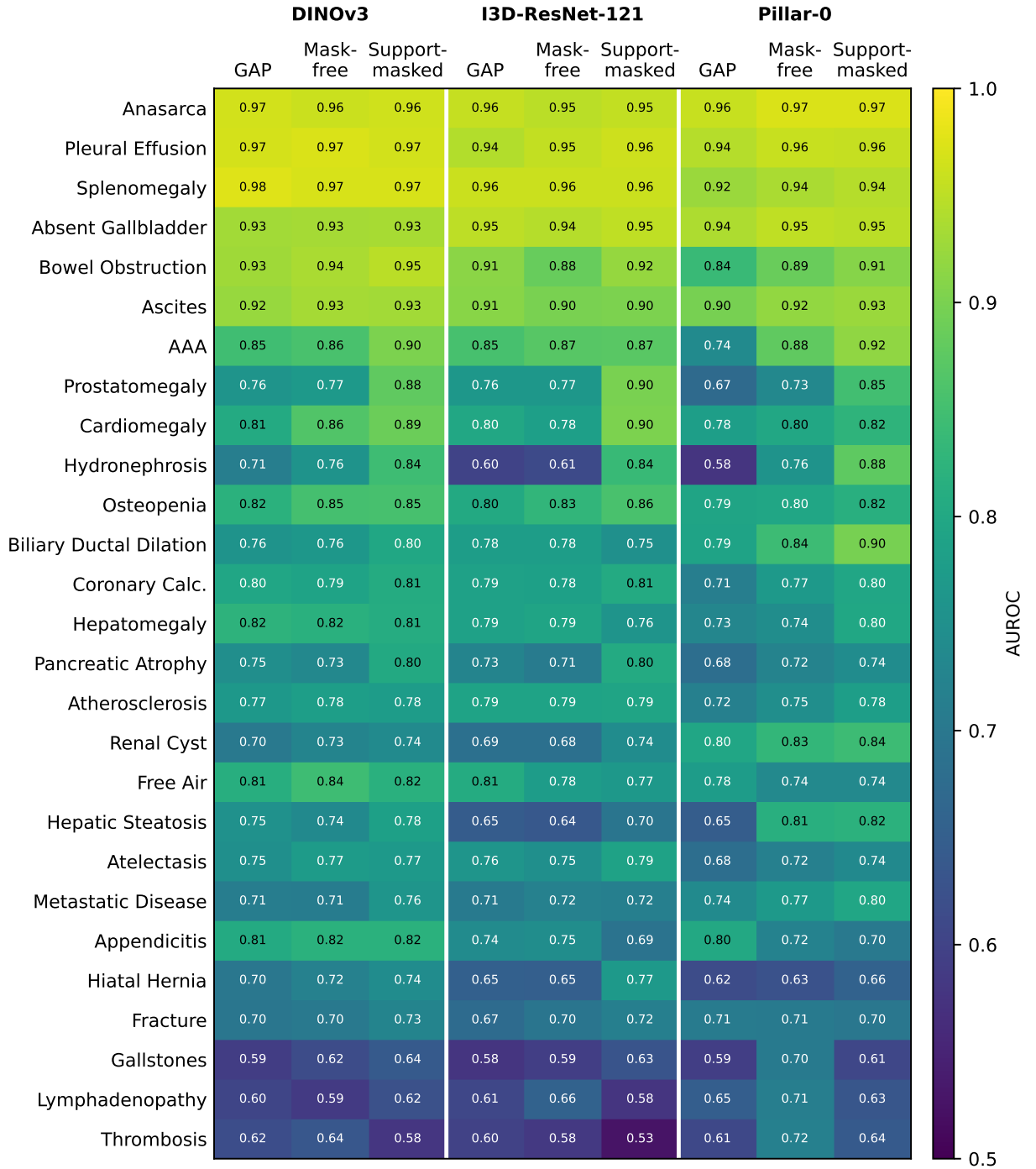


Figure S8: Absolute per-disease MERLIN-to-Duke transfer on the shared 27-label subset. Heatmap of absolute per-finding AUROC on Duke–Abdomen for the 27 findings shared between MERLIN and Duke–Abdomen. Rows correspond to disease labels and columns correspond to aggregation modes across DINOv3, I3D–ResNet-121, and Pillar-0: GAP, mask-free attention pooling, and support-masked pooling. Higher values indicate stronger frozen external discrimination after training on MERLIN. This figure provides the absolute disease-level AUROC values corresponding to the Δ AUROC heatmap in the main manuscript.

MERLIN Label Prevalence by Split

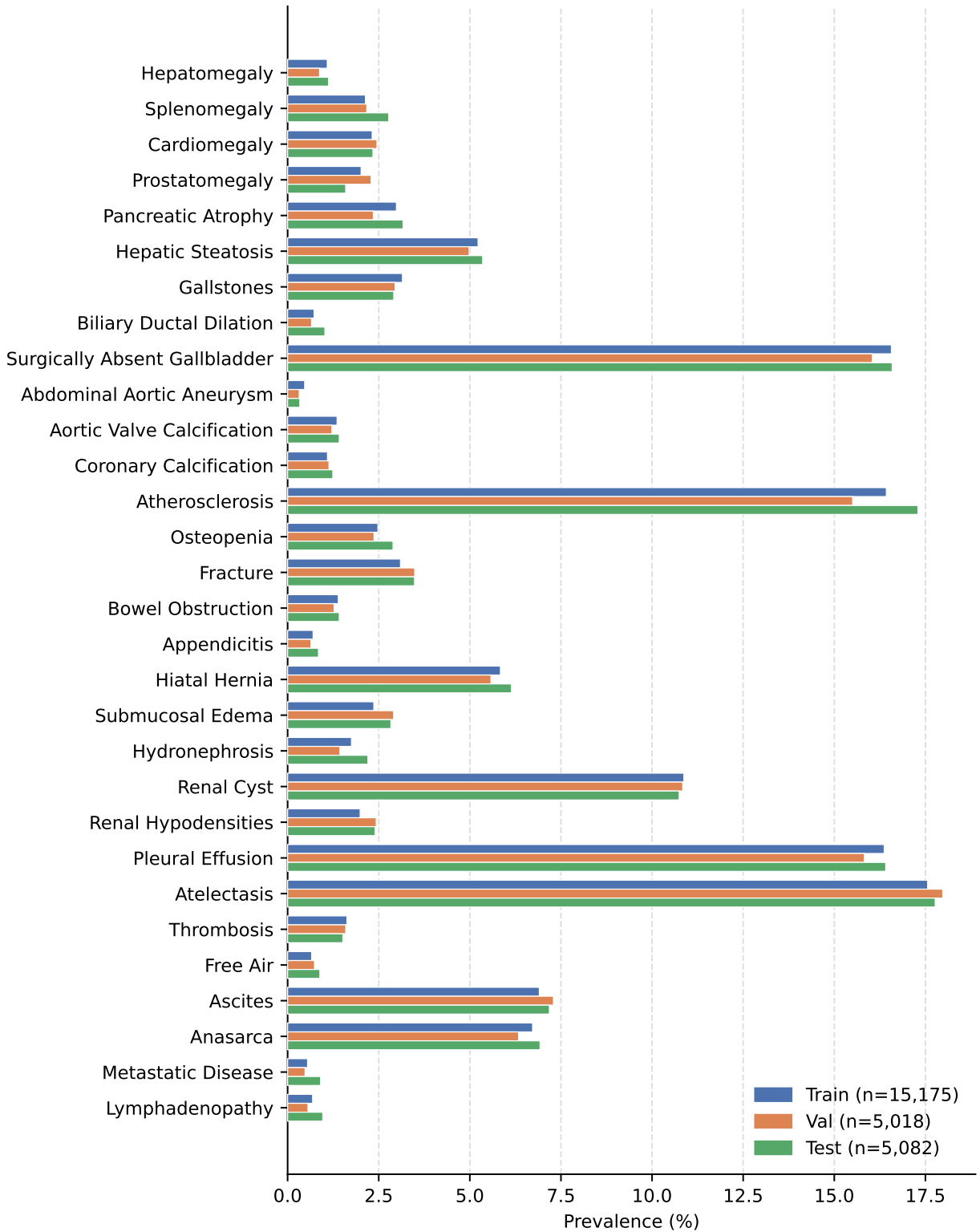


Figure S9: Label prevalence across MERLIN dataset splits. Prevalence (percentage of positive cases) for each of the 30 MERLIN findings across the training, validation, and test splits. Prevalence is computed as the fraction of cases labelled positive (= 1) out of all cases in each split, including those with missing annotations (= -1).